# Surface and Photochemistry

## (BL1A, 2B1, 4A1, 4A2, 5A, 5B, 8A)

(BL-1A)

# Characteristics of Photoresist for X-ray lithography

N. Sakai[a], K. Tada[a], Y. Utsumi[b] and T. Hattori[b]

[a]Toyo Gosei CO., LTD. Photosensitive Materials Research Center, 4-2-1 Wakahagi, Inba, Inba-gun, Chiba 270-1609 JAPAN
[b]Himeji Institute of Technology, Laboratory of Advanced Science and Technology for Industry
3-1-2 Koto, kamigori, Ako, Hyogo 678-1205 JAPAN

## Introduction

Increasing needs for the microstructures with height of over a few hundreds micron have been widely spread in the many fields of micro systems such as high power microactuators, high sensitivity micro sensors and microprobe spectroscopy for nano technology. Thus microstructures with high aspect ratio add new functions, high integration, and increase the performance of the micro system devices. In order to fabricate high aspect ratio microstructures with high throughput productivity, LIGA (Lithographie, Galvanoformung and Abformung) process using synchrotron radiation is one of the most promising techniques [1]. LIGA process consists of three techniques: X-ray lithography, electroforming, and molding. On the lithography technique, polymethylmethacrylate (PMMA) has been used as a standard X-ray resist, however it restricts the process cost cut down due to the low photosensitivity. Generally, UV photoresists have been advanced in the viewpoint of photosensitivity and succeeded in applying to semiconductor fabrication processes. However, conventional UV resists, that has been developed mainly for thin film resists utilizing as etching masks, are difficult to apply for LIGA process. Few resist to fabricate the thick patterns, e.g. over a few hundreds micron thickness on LIGA process, are found in the present. We have improved the photosensitivity and optical property of the novel thick resist "TG-P" for X-ray LIGA processes. So far, TG-P is mainly evaluated with white X-rays in NEW SUBARU (BL-11). However, photoresist has an optimum wavelength region for exposure that attains a highest sensitivity with an excellent resolution. Thus, we have tried to investigate a photon energy regime that might influence on the photosensitivity of TG-P using the monochromatized X-rays of BL-1A of UVSOR.

## Resist design

PMMA has been known as a conventional X-ray resist. The photosensitivity of this "classic" positive resist is derived from the chain scission due to X-ray irradiation. And the reduction in polymer molecular weight lead to enhanced solubility of the exposed regions. Thus, photosensitive mechanism for PMMA leads to its high resolution, however, its sensitivity is fairly low. On the other hand, the concepts of chemical amplify resists have been investigated widely in order to improving sensitivity [2]. One of these has been used to design a number of negative resists based on acid catalyzed cationic polymerization of crosslinking of polymers [3]. This concept has been utilized for the achievement of the ultra thick negative resist with high sensitivity. We have successfully designed and synthesized TG-P with mass production processes. Fig. 1 shows the honeycomb pattern profiles of TG-P achieved by deep X-ray lithography (New SUBARU).

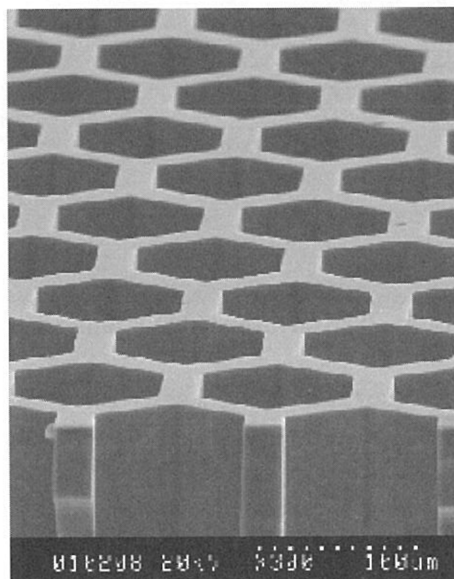

**Fig. 1. The honeycomb patterning profiles fabricated with TG-P. Line width: 20μm, resist thickness: 160μm**

## Experiments and Results

On the chemical amplify resist system, a photosensitive component has an important role that controls a photosensitivity though its content in photoresist is very low. The photosensitive component of TG-P is a photo acid generator that includes some sulfur atom in its molecule, and the photochemical decomposition with X-ray radiation can be occurred at the sulfur and a carbon bond. So, we examined the photosensitivity of TG-P to compare to expose two lights of different wavelengths, which one is a excitation light of sulfur (1s orbital) at 2472eV and the other is at 2400eV that is lower than the absorption edge of a sulfur atom.

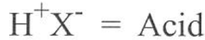


**Fig. 2. Reaction of photosensitive material by radiation exposure**

The TG-P handling process for X-ray exposure is shown as following.

Substrate: 100mm silicon wafer, Coating: spin-coat, Soft Bake: 95ºC/3 min.
Crystal: InSb (111), Post Exposure Bake (PEB): 95ºC/10min.
Development: Dip (with organic solvent)

Table 1 shows absorptions of TG-P film and exposure doses at each energy.

**Table 1. Absorptions of TG-P film and exposure doses**

| Sample | Photon Energy | Absorption[1)] | Normalized Absorption | Photon Flux (Photons/s/100mA) | Exposure Dose |
|---|---|---|---|---|---|
| A | 2472eV | 6.348% | 100% | $5\sim6\times10^8$ | 73.5A/min. |
| B | 2400eV | 6.787% | 106.92% | $6\times10^8$ | 74A/min. |

[1)]: The value was numerically estimated.

After development, both samples were cured by the x-ray exposure and the followed bake (PEB). Fig. 3 shows the surface images of the optical microscope for both samples after the PEB. As shown, clear morphology difference was observed among their surfaces.

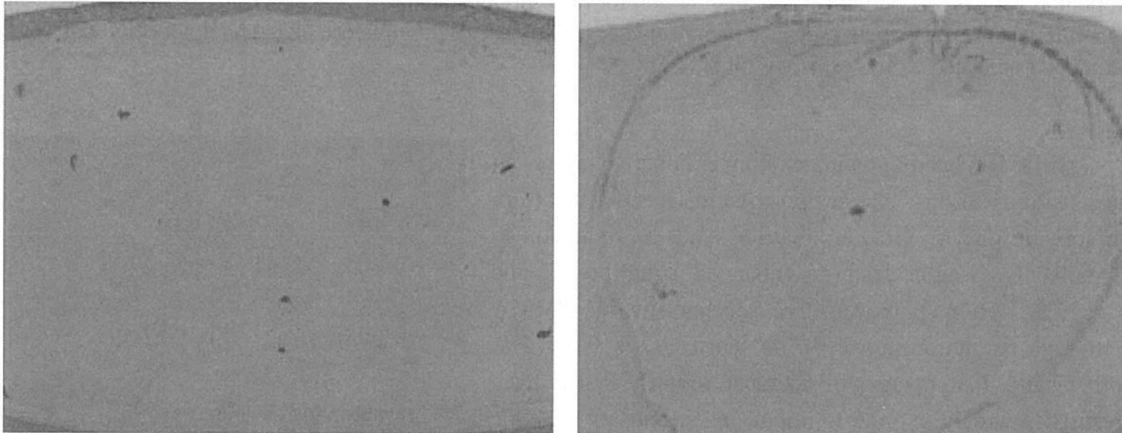

**Fig. 3. The pictures of TG-P films after development: Left (Sample-A), Right (Sample-B)**

Many wrinkles were observed only on the surface of the sample-B film. These were supposed to be caused by swelling with developer soakage and this suggests that the yields of the photochemical reaction increased by the excitation of sulfur atom. This acceleration leads to the higher photosensitivity for the photoresists. According to this result, it was suggested that the photosensitivity of photoresist for X-ray lithography depends on the photon energy near the absorption edge of the elements in the photo acid generator. It is important to choose the optimum elements in the photo acid generator of which absorption edges exist within the region of the x-ray spectrum to use in order to design high sensitive photoresists.

**References**


1. E. L. Becker, *et. al., Microelectron. Eng.,* 4, pp.35-42 (1982)
2. Ito H., Willson C. G., *Proc. Reg. Tech. Conf.* on "Photopolymers, Principles, Process and Materials", Mis-Hunson Sect. SPE, Nov. 8-10, p.331 (1982)
3. Crivello, J. V., *Proc. SPE Reg. Tech. Conf.* on "Photopolymers, Principles, Process and Materials", Nov. 8-10, Eiienville, N.Y. pp.267 (1982)

(BL2B1)

# Orientation of Adsorbed Nitrogen and Nitrous Oxide on Palladium (110) at Low Temperatures

H. Horino,[a] I. Rzeznicka,[a] T. Matsushima,[b] K. Takahashi,[c] E. Nakamura[c]

[a] *Graduate School of Environmental Earth Science, Hokkaido University, Sapporo 060-0810, Japan*
[b] *Catalysis Research Center, Hokkaido University, Sapporo 060-0811, Japan*
[c] *Institute for Molecular Science, Myodaiji Okazaki 444-8585, Japan*

The orientation of adsorbed $N_2O$ and $N_2$ was examined at around 60 K on Pd(110) by near-edge X-ray absorption fine structure (NEXAFS). Adsorbed $N_2$ stands on the surface; the $\pi$ resonance peak at 401 eV of the photon energy decreased with increasing X-ray incidence angle when its polarization was in a plane along either the [001] or $[1\bar{1}0]$ direction, and the $\sigma$ resonance at around 420 eV was observable only at grazing angles. On the other hand, for $N_2O$(a), two $\pi$ resonance peaks were observed at 401 and 405 eV. With increasing X-ray incident angle, their intensities increased significantly when the polarization was in a plane the [001] direction, and the intensities decreased for the polarization in the $[1\bar{1}0]$ direction. The orientation of $N_2O$ was discussed.

## Introduction

Catalytic $N_2O$ decomposition on palladium surfaces has attracted much attention because $N_2O$ is a major by-product in catalytic NO decomposition and yields a remarkable greenhouse effect. This species was recently identified as the intermediate emitting $N_2$ in NO decomposition on Pd(110). Furthermore, it is mostly decomposed on Pd(110) below 150 K and emits $N_2$ in an inclined way in the plane along the [001] direction [1,2]. Thus, $N_2O$(a) oriented along the [001] direction was proposed to be the precursor of the dissociation. Recent DFT calculations by Kokalj show that $N_2O$(a) oriented along the [001] direction is as stable as the standing form with a bonding through the terminal nitrogen to metal [3]. Infrared reflection absorption spectroscopy work reports the standing form, but it is insensitive to the lying form. This reports the X-ray incident angle dependence of the $\pi^*$ resonance of $N_2O$ when the electric vector is in the plane either along the [001] or the $[1\bar{1}0]$ directions.

## Experimental

The angle of X-ray incidence ($\theta$) with respect to the surface normal was varied by rotating a Pd(110) crystal such that the electric vector of the X-ray, ***E***, was oriented in a plane parallel to or perpendicular to the $[1\bar{1}0]$ direction. The crystal was kept at around 60 K by liquid helium cooling during the NEXAFS measurements. The NEXAFS spectra were recorded in a partial Auger electron yield mode with the kinetic energy of the nitrogen KLL Auger electrons at 382 eV.

## Results and Discussion

On the clean surface, no signal peaks were found in a raw NEXAFS spectrum in the photon energy range from 395 eV to 410 eV. Above this level, however, the signal due to Pd became significant. Thus, the signal at 410 eV was used to normalize the observed spectra in the partial Auger electron yield mode. The $N_2O$ coverage, $\Theta_{N2O}$, was determined by thermal desorption.

**[$N_2$(a)]** NEXAFS of $N_2$(a) exhibits two resonance states at the present mono-chromator, *i.e.,* $\pi^*$ at 401 eV and $\sigma^*$ at 413-430 eV. The $\pi$ resonance decreased with increasing incidence angle of X-ray and was mostly suppressed at around $\theta = 80^\circ$. On the other hand, the $\sigma$ resonance became visible at grazing angles. Similar results were obtained when the X-ray polarization was in a plane along either the [001] or $[1\bar{1}0]$ direction. No coverage dependence was found. $N_2$(a) always stands on the surface.

**[$N_2O$(a)]** Two resonance states were fund in NEXAFS at 401.3 and 404.7 eV when the surface was exposed to $N_2O$ at 60 K. The former was assigned to the transition from the 1s state of the terminal nitrogen atom ($N_t$) to $3\pi^*$, and the latter due to the excitation of a 1s electron of the center nitrogen ($N_c$). This energy difference of 3.4 eV and similar intensity of both peaks agree with those of gaseous $N_2O$, confirming a molecular form of $N_2O$(a). The signal ratio did not change with $N_2O$ exposure. On the other hand, the $\sigma$ resonance at around 425 eV became very weak and visible only at grazing angles. Typical raw spectra at $\theta = 10^\circ$ are summarized at various coverage in Fig. 1.

The $\pi$ resonance originating from the $N_c$ 1s decreased to about 80 % at the grazing angles when the polarization was parallel to the $[1\bar{1}0]$ direction (Fig. 2a). The other $\pi$ resonance from the $N_t$ 1s decreased to about 70 %. The former $\pi$ resonance originating from the $N_c$ 1s increased by about 70 % with increasing incident angle to the grazing angle when the

polarization was oriented in a plane along the [001] direction (Fig. 2b). On the other hand, the other π resonance from the $N_t$ 1s was fairly constant.

Two adsorption forms, a standing and a lying into the [001] direction, have been predicted by DFT results [3]. The π resonance should decrease in a form of $\cos^2\theta$ with increasing the incident angle when $N_2O$ stands, whereas the signal would increase in a form of $\sin^2\theta$ when $N_2O$ is lying along the polarization direction. A typical deconvolution is shown by the dotted curves in Fig. 2b, where only a lying form along the [001] direction and a standing form are assumed. In Fig. 2a, the contribution from the standing form (the dotted curve) is first subtracted and the remaining signal is drawn by the broken curve. The remaining signal is significant at the normal incidence and increases with increasing incident angle, although it should be constant when the transition probability from 1s to 3π* is the same for the surface parallel and perpendicular π* orbital. The contribution from another lying form oriented along the [$1\bar{1}0$] direction must be considered.

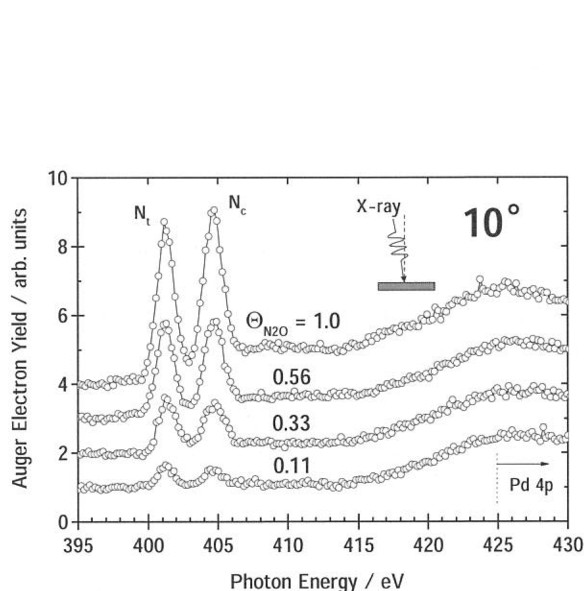


Fig. 1. NEXAFS spectra of $N_2O$ ad-molecules at an incidence angle of 10°. The electric vector ***E*** was in a plane along the [001] direction.

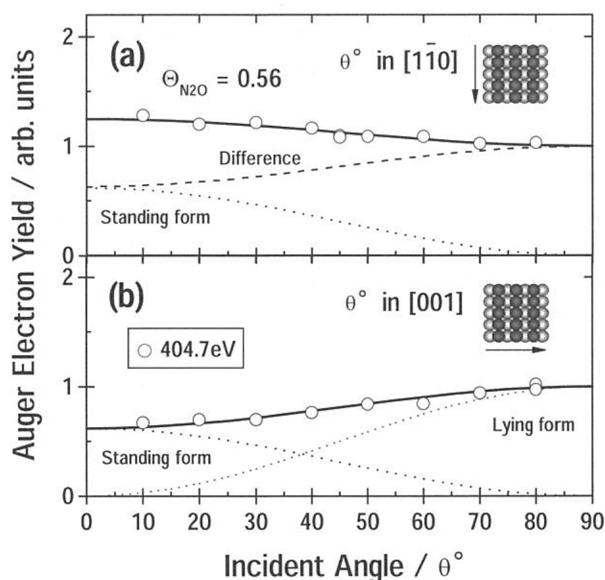


Fig. 2. X-ray incident angle dependence of π resonance of $N_2O$(a). The electric vector ***E*** was in a plane along (a) the [$1\bar{1}0$] and (b) the [001] direction. The deconvolution into a standing form and a lying along the [001] direction is given in (b). The deconvolution in (a) is explained in the text.

* This work was supported in part by Grant-in-Aid No. 13640493 for General Scientific Research from the Japan Society for the Promotion of Science.

**References**


1 Y. Ohno, I. Kobal, H. Horino, I. Rzeźnicka, T. Matsushima, *Appl. Surf. Sci.* **169/170**, 273 (2001).
2 H. Horino, S. Liu, A. Hiratsuka, Y. Ohno, T. Matsushima, *Chem. Phys. Lett.* **341**, 419 (2001).
3 A. Kokalj, I. Kobal, H. Horino, Y. Ohno, T. Matsushima, *Surf. Sci.* **506** (2002) 196.
4 H. Horino, S. Liu, M. Sano, S. Wako, Y. Ohno, A. Hiratsuka, T. Matsushima, *Topics in Catal.* **18** (2002) 21.

(BL2B1)

# Dissociation and Orientation of Adsorbed Nitrous Oxide on Rhodium (110) at Low Temperatures

H. Horino,[a] I. Rzeznicka,[a] T. Matsushima,[b] K. Takahashi,[c] E. Nakamura[c]

[a] *Graduate School of Environmental Earth Science, Hokkaido University, Sapporo 060-0810, Japan*
[b] *Catalysis Research Center, Hokkaido University, Sapporo 060-0811, Japan*
[c] *Institute for Molecular Science, Myodaiji Okazaki 444-8585, Japan*

The orientation of adsorbed $N_2O$ was studied at 60 K on Rh(110) by near-edge X-ray absorption fine structure (NEXAFS). At high exposures, $N_2O$(a) showed two $\pi$ resonance peaks at 401 and 405 eV. The former was fairly constant and the latter decreased to about 50% over the incident angle of 0° to the grazing angle of 80° when the X-ray polarization was in a plane along either the [001] or [1$\bar{1}$0] direction. At small exposures, only one $\pi$* resonance at 401 eV was clearly observed and its polarization dependence was very similar to that of $N_2$(a) indicating dissociation of $N_2O$. Adsorbed $N_2$ stands on the surface.

**Introduction**

Catalytic $N_2O$ decomposition on rhodium surfaces has attracted much attention because $N_2O$ is a major by-product in catalytic NO decomposition on this best metal catalyst and yields a remarkable greenhouse effect. This species was recently identified as the intermediate emitting $N_2$ in NO decomposition on Pd(110) [1,2]. Furthermore, it is mostly decomposed on Rh(110) below 120 K and emits $N_2$ in an inclined way in the plane along the [001] direction. $N_2O$(a) oriented along the [001] direction was proposed to be the precursor of the dissociation. Recent DFT calculations by Kokalj show that $N_2O$(a) oriented along the [001] direction is as stable as the standing form with a bonding through the terminal nitrogen to metal [3]. This first reports the X-ray polarization dependence of the $\pi$* resonance of $N_2O$ on Rh(110).

**Experimental**

The angle of X-ray incidence ($\theta$) with respect to the surface normal was varied by rotating a Rh(110) crystal such that the electric vector of the X-ray, ***E***, was oriented in a plane parallel to or perpendicular to the [1$\bar{1}$0] direction. The crystal was kept below 60 K by liquid helium cooling during the NEXAFS measurements. The NEXAFS spectra were recorded in a partial Auger electron yield mode with the kinetic energy of the nitrogen KLL Auger electrons at 382 eV. The sample crystal was heated to 1200 K to remove remaining surface oxygen after standard cleaning procedures.

**Results**

On the clean surface, no signal peaks were found in a raw NEXAFS spectrum in the photon energy range from 395 eV to 410 eV. Thus, the signal at 410 eV was used to normalize the observed spectra in the partial Auger electron yield mode. The $N_2O$ coverage, $\Theta_{N2O}$, was determined by thermal desorption.

**[$N_2$(a)]** NEXAFS of $N_2$(a) exhibits two resonance states at the present mono-chromator with an energy resolution of 0.5 eV, *i.e.*, $\pi$* at 401 eV and $\sigma$* at 420±4 eV. The $\pi$ resonance decreased with increasing incidence angle of X-ray and was mostly suppressed at around $\theta = 80^\circ$. On the other hand, the $\sigma$* resonance became visible at grazing angles. These phenomena were very similar for the X-ray polarization in a plane either along the [001] or [1$\bar{1}$0] directions. $N_2$(a) stands on the surface.

**[$N_2O$(a)]** Two $\pi$* resonance states were found in NEXAFS at 401.2 and 404.7 eV with a similar intensity when the surface was exposed to $N_2O$ to saturation at 60 K (Fig. 1). The former is due to the transition from the 1s state of the terminal nitrogen atom ($N_t$) to 3$\pi$*, and the latter due to the excitation of a 1s electron of the center nitrogen ($N_c$) to 3$\pi$*. This energy difference of 3.5 eV and their similar intensity agree with those of gaseous $N_2O$, confirming a molecular adsorption form. At small coverage, however, the spectrum changed largely (Fig. 2). The peak at 405 eV was small, and the other at 401 eV was still intense and decreased with increasing incident angle in a way similar to that of $N_2$(a). This was assigned to adsorbed product $N_2$ from dissociative adsorption of $N_2O$. At $\Theta_{N2O}$=0.75, the signal at 405 eV decreased slowly with increasing the incidence angle (Fig. 3b,c) whereas the signal at 401 eV decreased to about 55-65 % because of the contribution from the signal due to $N_2$(a).

## Discussion

The π resonance intensity must change sharply with X-ray incidence angle when the N-N bond is oriented only in a definite direction. The observed π resonance at 405 eV, however, was insensitive to the incidence angle. Recent DFT work predicts two adsorption forms, i.e., a standing form and a lying one along the [001] direction [3]. In the model with only the lying form, the signal would increase with incident angle along the [001] direction and remain constant along the $[1\bar{1}0]$ direction. However, the observed signal was fairly constant in both directions, indicating the presence of the standing form and the lying form oriented along the $[1\bar{1}0]$ direction.

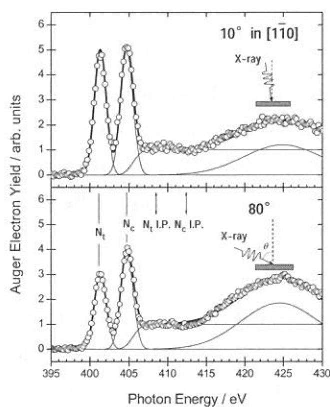


Fig. 1. NEXAFS spectra of $N_2O(a)$ at saturation. The incidence angle (θ) of 10° and 80°. The electric vector ***E*** was in a plane in the $[1\bar{1}0]$ direction.

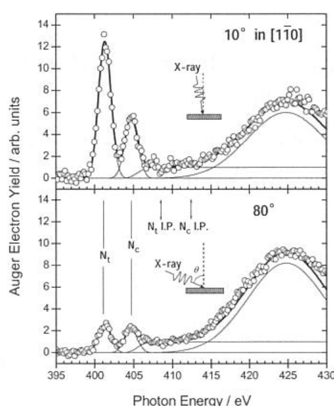


Fig. 2. NEXAFS spectra of $N_2O(a)$ at $\Theta_{N2O}$ = 0.25. The incidence angle (θ) of 10° and 80°. The electric vector ***E*** was in a plane in the $[1\bar{1}0]$ direction.

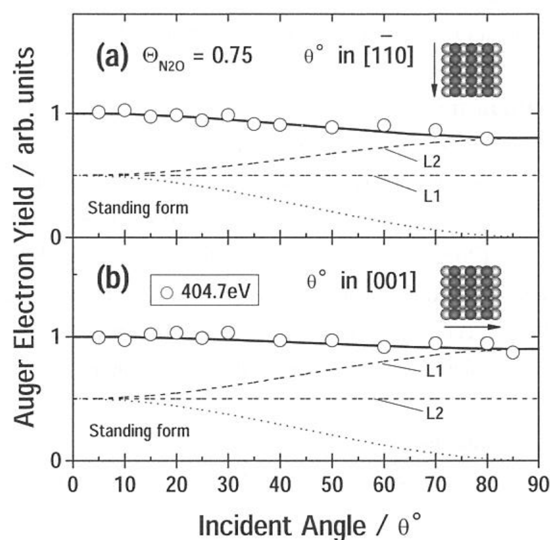


Fig. 3. The polarization dependence of the π resonance of $N_2O$ at $\Theta_{N2O}$ = 0.75 for the polarization in a plane along (a) the $[1\ \bar{1}\ 0]$ and (b) the [001] direction. Typical deconvolutions into the standing form is shown by dotted curve. L1 and L2 shown by broken curves stand for a lying $N_2O(a)$ oriented along the [001] and $[1\bar{1}0]$, respectively. The solid indicates the sum of these curves.

* This work was supported in part by Grant-in-Aid No. 13640493 for General Scientific Research from the Japan Society for the Promotion of Science.

## References

[1] H. Horino, I. Rzeźnicka, A. Kokalj, I. Kobal, T. Matsushima, A. Hiratsuka and Y. Ohno, J. Vac. Sci. Technolog. **20** (2002) 1592.
[2] T. Matsushima, Catalysis Surveys from Japan, **5** (2002) 71.
[3] A. Kokalj, I. Kobal, H. Horino, Y. Ohno, T. Matsushima Surf. Sci., **506** (2002) 196.

(2B1)

# $H^+$ Desorption Induced by $4a_1 \leftarrow$ O:1s Resonant Transitions of Condensed Water Studied by Electron – Polar-Angle-Resolved-Ion Coincidence Spectroscopy

Kouji ISARI[*1], Eiichi KOBAYASHI[*2,*3], Masanobu MORI[*4], Kazuhiko MASE[*2], Koji OKUDAIRA [*4,*5,*6], Kenichiro TANAKA[*1], Nobuo UENO[*4,*6], Shin-ichi NAGAOKA[*7]

[*1] *Graduate School of Science, Hiroshima University, 1-3-1 Kagamiyama, Higashi-Hiroshima 739-8526, Japan*
[*2] *Institute of Materials Structure Science, 1-1 Oho, Tsukuba 305-0801, Japan*
[*3] *Present address; National Institute of Advanced Industrial Science and Technology, Tsukuba Central 5, 1-1-1 Higashi, Tsukuba 305-8565, Japan*
[*4] *Graduate School of Science and Technology, Chiba University, 1-33 Yayoi-cyo, Inage-ku 263-8522, Japan*
[*5] *Institute for Molecular Science, 38 Nishigounaka, Myodaiji-cho, Okazaki 444-8585, Japan*
[*6] *Faculty of Engineering, Chiba University, 1-33 Yayoi-cyo, Inage-ku 263-8522, Japan*
[*7] *Department of Material Science, Ehime University, 2-5 Bunkyo-cyo, Matsuyama 790-8577, Japan*

For $H^+$ desorption induced by $4a_1 \leftarrow$ O:1s resonant transitions of condensed water ($H_2O$) we have proposed a four-step $H^+$ desorption mechanism: (1) the $4a_1 \leftarrow$ O:1s transition, (2) extension of HO-H distance in the $(O{:}1s)^{-1}(4a_1)^1$ state (ultra-fast O-H extension), (3) a spectator Auger transition leading to a two-hole state with an excited electron in the $4a_1$ orbital, and (4) $H^+$ desorption taking place in turn (**Fig. 1**) [1]. To clarify the details of the $H^+$ desorption mechanism we investigated the phenomena by using electron – polar-angle-resolved-ion coincidence spectroscopy which offers information on desorption polar angle and kinetic energy distributions of ions for selected Auger-final-states [2].

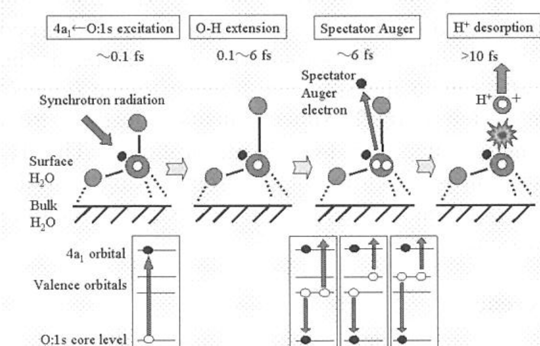


**Fig. 1.** Four-step $H^+$ desorption mechanism for $4a_1 \leftarrow$ O:1s resonance of condensed $H_2O$: (1) $4a_1 \leftarrow$ O:1s transition, (2) extension of the HO-H distance in the $(O{:}1s)^{-1}(4a_1)^1$ state, (3) a spectator Auger transition leading to a two-hole state with an excited electron in the $4a_1$ orbital, and (4) $H^+$ desorption. The $H^+$ desorption is driven mainly by the O-H repulsive potential surface of the $(O{:}1s)^{-1}(4a_1)^1$ state.

**Fig. 2** shows total ion yield (TIY, corresponding to the $H^+$ yield) and Auger electron yield (AEY) spectra of condensed $H_2O$. Since the peak of kinetic energy distribution of $H^+$ at $4a_1 \leftarrow$O:1s resonant excitation is located in 3-4 eV [3], the anode 1 mainly detects $H^+$ desorbed in the polar angle of 0-17° from the surface normal while the anode 2 detects $H^+$ in the polar angle of >20°. On the other hand, ion was scarcely detected in the anode 3. This result shows that desorption polar angle of $H^+$ is not so large, which is consistent with the report by Coulman et al. [3]. The peak observed in the TIY spectra at hv = 532.6-533.6 eV was assigned to the $4a_1 \leftarrow$O:1s resonant transition of surface $H_2O$ [1, 4]. The $4a_1 \leftarrow$O:1s resonant peak in TIY for the anode 2 was, however, smaller than that for the anode 1. On other hand, the TIY spectra in the other photon energy range were almost the same between the anode 1 and anode 2. The difference suggests that $H^+$ desorption mechanisms involved at the $4a_1 \leftarrow$O:1s resonance are somehow different between the surface

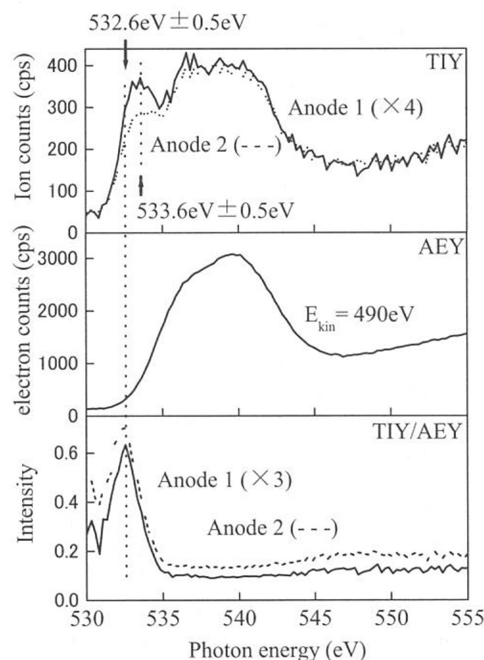


**Fig. 2** Total ion yield (TIY) with the anode 1 (solid line) and the anode 2 (dashed line), Auger electron yield (AEY, electron kinetic energy ($E_{kin}$) = 490 eV), and TIY/AEY spectrum with the anode 1 (solid line) and the anode 2 (dashed line) of condensed $H_2O$.

normal and off-normal directions.

**Fig. 3** shows Auger electron spectra and Auger electron – polar-angle-resolved ion coincidence yield spectra at the $4a_1$←O:1s resonance. In the coincidence yield spectrum for the anode 1, the $H^+$ coincidence yield was enhanced at the Auger electron kinetic energy (KE) of 505 eV, while intense peak was not observed for KE < 500 eV. On the other hand, the $H^+$ coincidence yield at KE = 505 eV was relatively decreased while the peaks were observed at KE = 485 eV and 460 eV in the spectrum for the anode 2. The latter feature of the $H^+$ coincidence yield spectrum for the anode 2 is similar to that of the normal Auger electron – photoion (AEPICO) yield spectrum at O:1s ionization of condensed $H_2O$ [5]. The summation of the coincidence yield of the anode 1 and anode 2 reproduced the $H^+$ AEPICO yield spectrum measured by the previous polar-angle-integrated EICO analyzer with a single-anode TOF-MS [6]. These results suggest that another ion desorption mechanism exists for $H^+$ desorbed in the larger polar angles at the $4a_1$← O:1s resonance.

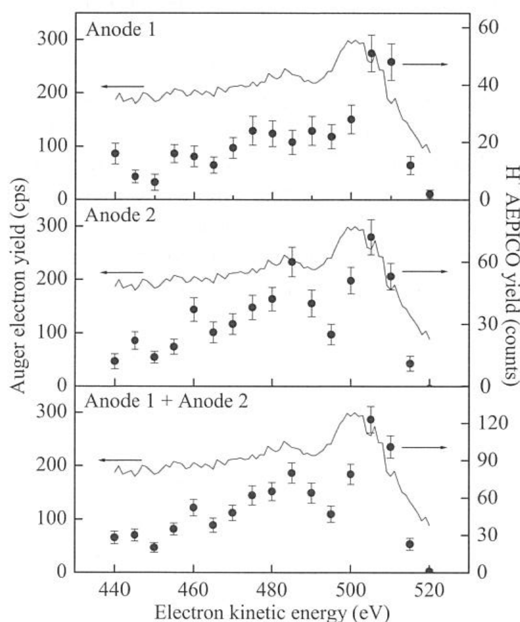


**Fig. 3** Auger electron spectra (solid line) and Auger electron - $H^+$ photoion coincidence yield spectra (closed circles) at the $4a_1$ ← O:1s resonance of condensed $H_2O$.

**Fig. 4** shows $H^+$ coincidence yield spectra normalized by dividing the yield by the ion count for the individual anode. It shows that the coincidence yield for the anode 2 is overall fewer than that for the anode 1, and that peak intensity at KE = 505 eV of the anode 1 is twice as large as that for the anode 2.

A probable candidate for another $H^+$ desorption mechanism is $H^+$ desorption induced by normal O:KVV Auger processes following ultrafast $4a_1$ electron transfer into the substrate as shown in **Fig. 5**. This mechanism is not negligible when the lifetime of the $4a_1$ electron is comparable with that of the O:1s core hole. $H^+$ desorption induced by normal O:KVV is know to show a larger polar angle distribution than that at $4a_1$ ← O:1s resonance [3].

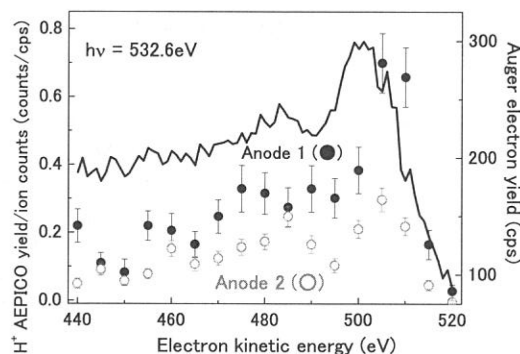


**Fig. 4** $H^+$ coincidence yield spectra normalized by dividing the yield by the ion count for the individual anode.

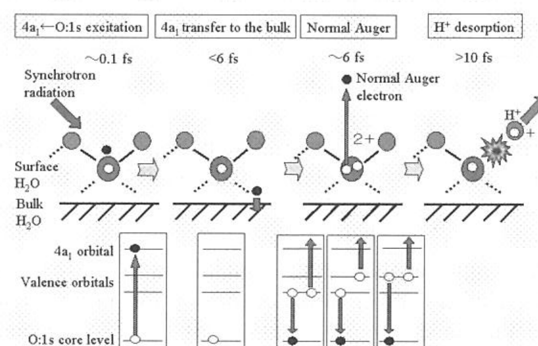


**Fig. 5.** Another possible four-step $H^+$ desorption mechanism for the $4a_1$ ← O:1s resonance of adsorbed $H_2O$: (1) $4a_1$ ← O:1s transition, (2) transfer of the $4a_1$ electron to the substrate leading to the $(O:1s)^{-1}$ state, (3) a normal Auger transition leading to a two-hole state, and (4) $H^+$ desorption. The $H^+$ desorption is driven by the electron missing from the O-H bonding orbitals and effective Coulomb repulsion.

## References

[1] K. Mase, M. Nagasono, S. Tanaka, T. Urisu, E. Ikenaga, T. Sekitani, and K. Tanaka, J. Chem. Phys. 108 (1998) 6550.

[2] E. Kobayashi, K. Isari, M. Mori, K. Mase, K. Okudaira, K. Tanaka, N. Ueno, S. Nagaoka, UVSOR Activity Report 2002 ** (2003).

[3] D. Coulman, A. Puschmann, U. Höfer, H.-P. Steinrück, W. Wurth, P. Feulner, and D. Menzel, J. Chem. Phys. 93 (1990) 58.

[4] K. Mase, M. Nagasono, S. Tanaka, T. Urisu, E. Ikenaga, T. Sekitani, and K. Tanaka, Surf. Sci. 390 (1997) 97.

[5] M. Nagasono, K. Mase, S. Tanaka, and T. Urisu, Chem. Phys. Lett. 298 (1998) 141.

[6] K. Mase, S. Tanaka, S. Nagaoka, and T. Urisu, Surf. Sci. 451 (2000) 143.

(BL2B1)

# Adsorption Process of Ammonia on Zn-terminated ZnO(0001)


K.Ozawa, T. Hasegawa, Y. Shirotori, K. Edamoto, K. Takahashi*

*Department of Chemistry and Materials Science, Tokyo Institute of Technology, Ookayama, Meguro-ku, Tokyo 152-0033, Japan*

**Institute for Molecular Science, Myodaiji, Okazaki 444-8585*


Catalytic synthesis of ammonia ($NH_3$) has been one of the most-studied chemical reaction. $NH_3$ is also an important molecule as a reactant for nitric acid production under oxide-supported metal catalysts. Thus, it is important to elucidate the interaction manner of $NH_3$ with metal and metal-oxide surfaces from the industrial point of view.

Ammonia adsorption on low-index surfaces of single crystal ZnO has been the subject of both theoretical and experimental studies. Our recent photoelectron spectroscopy (PES) and near-edge X-ray absorption fine structure (NEXAFS) spectroscopy studies have shown that ammonia adsorbs molecularly on the non-polar ZnO($10\bar{1}0$) surface at room temperature with the $C_{3v}$ molecular axis tilted by 33°–41° from the surface normal direction.[1] On the other hand, it has been reported that partially decomposed ammonia is formed along with molecular species on the Zn-terminated ZnO(0001) surface even at 130 K.[2] However, detailed information about the ratio of the decomposed species to molecular ammonia, the decomposition process, etc. has not been available so far. In the present study, we have carried out the PES study in order to reveal details of the adsorption process of $NH_3$ on the Zn-terminated ZnO(0001) surface and have compared the results with the recent study for the $NH_3$/ZnO($10\bar{1}0$) system.

The PES measurements were performed at beam line 2B1. Synchrotron radiation was monochromatized by a grasshopper monochromator. The ultrahigh vacuum (UHV) chamber at the end of the beam line was equipped with a double-pass cylindrical mirror analyzer, low-energy electron diffraction (LEED) optics and a quadrupole mass spectrometer. The base pressure of the UHV system was less than $2 \times 10^{-10}$ Torr. For $NH_3$ adsorption, research-grade gas was introduced into the chamber through a variable leak valve. $NH_3$ adsorption and the PES measurements were carried out at room temperature.

Fig. 1 shows the change in the N 1s core-level spectrum of the $NH_3$-dosed ZnO(0001) surface as a function of $NH_3$ exposure. The inset shows the integral intensity of the N 1s peak which is extracted from the observed spectrum after a polynominal background (shown by dashed lines) is subtracted from each observed spectrum. The N 1s peak grows rapidly at low exposure ($< 2$ L), and the increasing rate diminishes for higher exposure. The growth of the peak intensity saturates at 20–30 L, suggesting the saturation of $NH_3$ adsorption at this exposure range.

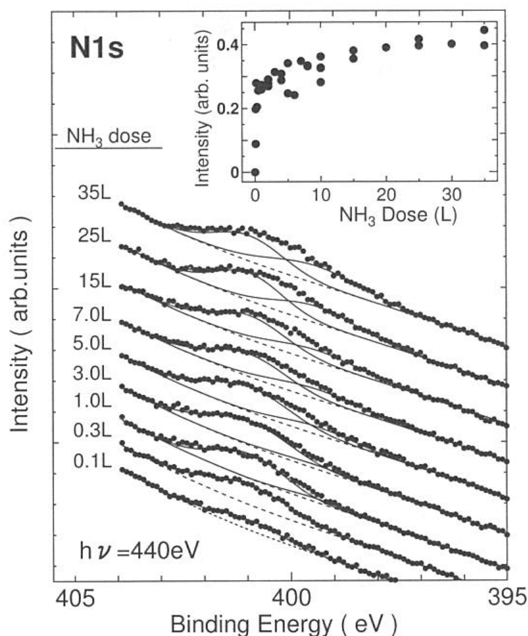


Figure 1: Change in the N 1s core-level spectrum of the ZnO(0001) surface exposed to ammonia at room temperature. Each spectrum was decomposed utilizing Gaussian functions after a polynominal-type background (dashed line) was subtracted from the observed spectrum. The inset shows the total N 1s peak intensity as a function of the $NH_3$ exposure.

In the initial stages of adsorption (0.1 and 0.3 L), the N 1s peak is composed of a single component with its peak maximum at 401.0 eV. At the exposure range greater than 1.0 L, a second component is observed at 399.3 eV. It is known that the N 1s peak from molecularly adsorbed ammonia on solid surfaces appears at 400–401 eV, whereas partially decomposed $NH_x$ ($x = 1, 2$) gives the N 1s peak at 398–399.4 eV.[3] Thus, the peak at

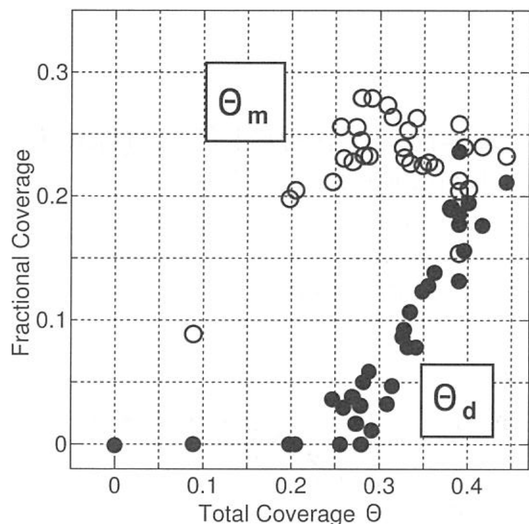


Figure 2: The plot of the fractional coverages of molecularly adsorbed ammonia $\Theta_m$ and partially decomposed ammonia $\Theta_d$ against the total coverage $\Theta$.

401 eV is associated with the molecularly adsorbed ammonia, while the decomposed $NH_x$ species are responsible for the 399.3-eV peak. This result is in sharp contrast to the result obtained for the $NH_3$/ZnO(10$\bar{1}$0) system, where decomposed species are not formed at room temperature.

The coverage $\Theta$ of ammonia (including both molecular and decomposed species) was estimated from the ratio of the N 1s peak intensity to the O 1s and Zn 4s peak intensities. The saturation coverage is found to be 0.5, which corresponds to $5.4 \times 10^{14}$ species/cm$^2$, i.e. a half of the number of the Zn atoms on the ideal (0001) surface. The saturation density of ammonia on ZnO(0001) is higher than that on ZnO(10$\bar{1}$0) ($3 \times 10^{14}$ cm$^{-2}$). This, together with the result that the $NH_x$ species are formed, indicates that the ZnO(0001) surface is more reactive for ammonia than the (10$\bar{1}$0) surface.

Fig. 2 shows the plot of the fractional coverages of $NH_3$ ($\Theta_m$) and $NH_x$ ($\Theta_d$) against the total coverage $\Theta$. It is clearly indicated that $\Theta_d$ starts to increase at $\Theta \simeq 0.25$. On the other hand, $\Theta_m$ increases linearly from the initial stages up to $\Theta = 0.25$ and turns to be in a decreasing trend for higher $\Theta$. Thus, the decomposed species are formed on the surface at the density of adsorbates higher than $2.7 \times 10^{14}$ cm$^{-2}$, where the average distance between adsorbates becomes shorter than 6.6 Å (note that no LEED patterns are observed at any $\Theta$, indicating an absence of ordered structures by adsorbates).

A recent scanning tunneling microscopy (STM) study for the atomic structure of the ZnO(0001) surface[4] has indicated that the intrinsically unstable polar (0001) surface is stabilized by introducing the O terminated steps with the amount so that the surface Zn/O atomic ratio becomes 0.75, i.e. the O coverages exposed to the surface is 0.25. Generally, these step edges are chemically active because of a high density of dangling bonds, and thus adsorption and decomposition of molecules should take place leadingly at the step edges. However, Fig. 2 suggests that the step edges on ZnO(0001) are not such active for deprotonation of ammonia at least in the initial stages of adsorption, since no decomposed species is formed. This is partly rationalized by the fact that, if $NH_3$ adsorbs on an atop site of a surface Zn atom at the side of the step edge with its $C_{3v}$ axis directing normal to the surface, the distance between the H atoms of ammonia and the O atoms in a step edge is as close as 2.5 Å. This distance is far longer than the typical O–H bond length of the hydroxyl group ($\sim$ 1 Å) but closer to the hydrogen bond length 2.9–3.2 Å. Thus, it is speculated that adsorbed $NH_3$ at the side of the step edges could be hydrogen-bonded with the step O atoms and does not undergo decomposition if molecule stands upright.

As $\Theta$ increases and the mean adsorbate–adsorbate distance decreases, a steric repulsion or a dipole-dipole repulsion between the adsorbates becomes large. These effects should be much more significant at $\Theta > 0.25$ than at $\Theta \leq 0.25$, since nearest-neighbor Zn sites must be occupied $\Theta > 0.25$ so that the adsorbate–adsorbate distance becomes 3.3 Å. Thus, in order to lessen the repulsive lateral interaction, the adsorbates should be inclined to some extent. At the step edges, if molecularly adsorbed ammonia is tilted towards the step edges at high $\Theta$, the deprotonation process can be operative upon shortening the H–O distance. Deprotonation of adsorbed ammonia on the terrace site is hardly expected, since it requires the involvement of the fully coordinated O atoms in the second layer. Therefore, decomposed species should be formed leadingly at the step edges rather than on the terrace. The observation that $\Theta_d$ at the saturation coverage does not exceed 0.25, which corresponds to the coverage of the O atoms exposed to the surface, seems reasonable for such a proposed decomposition mechanism. Absence of the decomposed species on the non-polar ZnO(10$\bar{1}$0) surface[1] should, thus, be due to the small density of step edges on the surface.[4]

[1] K. Ozawa *et al.* J. Phys. Chem. B 106 (2002) 9380.
[2] J. Lin *et al.* Inorg. Chem. 31 (1992) 686.
[3] E. Laksono, *et al.* Surf. Sci. 530 (2003) 37.
[4] O. Dulub *et al.* Surf. Sci. 519 (2002) 201; Phys. Rev. Lett. 90 (2003) 016102.

(BL2B1)

# EICO Study of the Ion Desorption induced by Valence and Inner-valnce Excitation from Ice

S. Tanaka[A], S. Nagaoka[B], K. Mase[C]

[A]*The institute of Scientific and Industrial Research, Osaka University, Ibaraki 567-0047, Japan*

[B]*Chemistry Group, Department of Fundamental Material Science, Faculty of Science, Ehime University, Matsuyama 790-8577, Japan*

[C]*Institute for Material Structure Science, Tsukuba 305-0801, Japan*

Desorption induced by the electronic transition (DIET), including electron-stimulated desorption (ESD) and photo-induced desorption (PSD), has bee studied for many decades because of its technological importance and interests in basic science. Electron-Ion Coincidence (EICO) technique has been recently developed for investigating the ion desorption induced by the core-level excitation. It was applied to many systems, and has shown that it is a very powerful tool for the core-level excitation phenomena. However, this technique can applied to not only the core-level excitation but also to the valence- and inner-valence excitation phenomena. In this report, we present the application of this technique to the ion-desorption from the ice surface, which is critically important from many aspects, and it is shown that the inner-valence excitation is crucial for the ion desorption from ice.

All the experiments were carried out the UHV chamber at BL2B1. The photon energy, provided by the grasshopper monochromator, was set to be 180eV. Amorphous ice was prepared by deposition on the Si substrate cooled with liquid nitrogen.

Figure 1 shows the photoelectron spectrum taken with the double-pass CMA. The three peaks at 160-180eV are ascribed to valence bands derived from the O2p and H1s electrons. They originate from the $H_2O$ molecular orbitals (MOs) of $1b_2$, $3a_1$, and $1b_1$ (from left to right). Other peaks around 148eV are ascribed to the O2s-derived inner-valence bands, which originates from the $2a_1$. This is splitted into two peaks. The small and broad structure around 130eV is ascribed to the shake-up satellite of the $2a_1$ peaks.

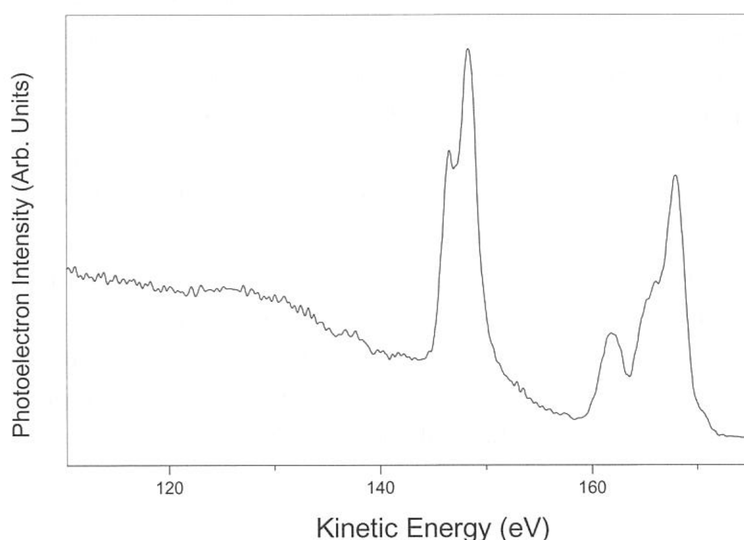


**Figure 1**

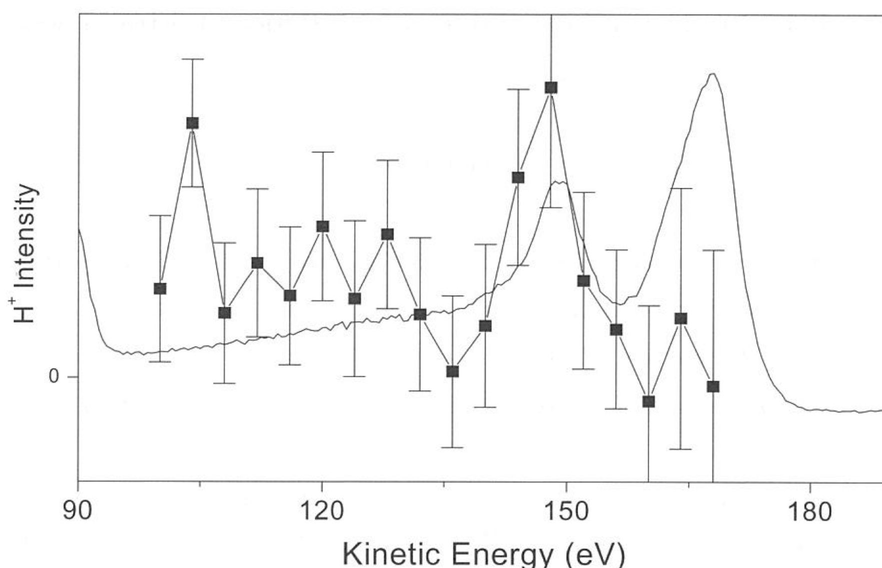


**Figure 2**

The photoelectron-photoion coincidence (PEICO) measurements were carried out at the same photon energy. Ions observed in the PEPICO spectra were only $H^+$. Figure 1 shows the photoelectron spectrum taken with the EICO appratus together with the $H^+$ intensity as a function of the kinetic energy of the electrons used as triggers in the coincidence measurements. Although the photoelectron spectrum in Fig.2 is broader than the one in Fig.1 taken with the double-pass CMA, the three features, which are the O2p-derived valence band, O2s-derived inner-valence band, and the small shake-up sattelite, are clearly observed as well. The increase observed at 90 eV is due to the Si-LVV Auger electron emission from the substrate.

The photon energy was lower than the O1s binding energy, and thus the desorption of $H^+$ should be due to the valence and inner-valence excitation. The intensity of $H^+$ in the coincidence spectra corresponds to the desorption probability assording to the previous EICO studies. This is almost zero at kinetic energies to be higher than 160eV. This indicates that the valence (O2p and H1s) excitation does not yield the $H^+$ desprtion on the ice surface. The $H^+$ intensity makes a peak at the kinetic energy corresponding to the inner-valence (O2s) excitation. A broad fearute at the kinetic energy corrsponding to the shake-up sattelite are also observed. These resutls suggest that the $H^+$ desorption is induced by the inner-valence excitation, and its shake-up excitation. Considering the relative intensity of the $H^+$ to the photoelectron peak, the desorption probability due to the shake-up excitation should be larger than that due to the innter-valence excitation. The desorption induced by the inner-valence excitation can be attributed to the two hole final state which is provided by the Auger decay of the O2s hole at the inner-valence band. The final state of the Auger decay of the shake-up excitation has three holes at the valence band, which may be a main reason for larger desprotion probability after the shake-up excition.

(BL4A1)

# SR Etching for Ti-contained Glass

Y. IMAIZUMI, E. MATSUMOTO[a)], H. YAMADA[a)], A. YOSHIDA[a)], T. URISU[b)], M. SUEZAWA, K. AWAZU[c)]

Institute for Materials Research, Tohoku univ., Katahira, Aoba-ku, Sendai, Japan
(a) Toyohashi univ. of Technology, Tempaku-cho, Toyohashi, Japan
(b)Institute for Molecular Science, Myodaiji, Okazaki, Japan
(c)National Institute of Advanced Industrils Science and Technology, Umezono, Tsukuba, Japan

A new glass containing Ti that can be etched by irradiation of synchrotoron radiation was found. It is expected that this special glass is used for the various useful application using synchrotron radiation.

In this experiment, we used the UVSOR BL-4A1 for etching light source. This line is available for double crystal monochromator, but this experiment was performed without monochromator. The ring current and exposure dose was monitored for reproducibility. The stainless steel through-hole mesh was used for a mask. This mesh has a hole of the 100$\mu$ m size. The glass sample was set on Si wafer chip for the 10x10 mm size, and clamped Tantalum film with the mask. For temperature controll, a K-type thermo-couple was used. In this experiment, the room temperature SR exposure was performed without any temperature control. At higher than 450K, the sample temperature was precisely controlled by using automatic temperature heating system. The Ti-contained glass sample was get from NIPPON-SHEET-GLASS co ltd.. The glass (0.3 mm thick) was cut for the size 10x10mm. The depth of the etched area was measured by using Dektak3 surface analysis system. Figure.1 shows the surface topography after SR etching. This indicates that only SR exposure, without etchant gas, induces the etching. The etching rate was about 0.5$\mu$ m / hour (total dose of about 10000mA・min). Figure. 2 show the dose dependence for the etched depth on the SR dose and the temperatures. The depth was saturated above about 10000 mA・min, however, in the dose of below 10000mA・min, the relation between the depth and the SR dose shows a complete linearity. In the case of the laser abrasion of conventional glass, it is reported that the etching rate is nonlinear. So, the observed linear relation for the SR etching of the Ti-containing glass is very interesting. The chemical analysis of the etched surface is now under investigation using a X-ray photoelectoron spectroscopy (XPS). In addition, when the sample temperature was increased, the etching rate was also increased.

In conclusions, It is found that the Ti-containing glass is etched by using the SR without any etching gases. It is expected that this SR glass etching will be available for various applications, especially, for nano-size glass etching.

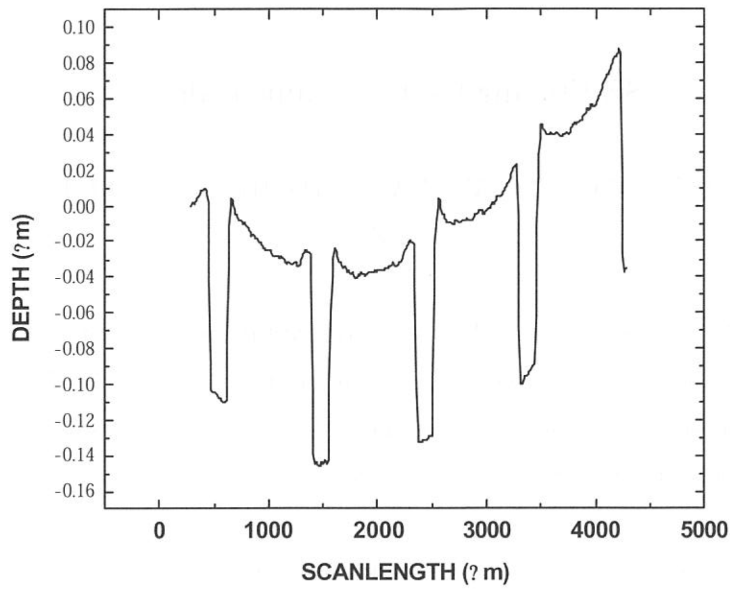


Fig.1 The depth profiles for the Ti-contained glass by using Dektak3 surface analysis system. Dose is 10000mA･min (about 1hour), white beam.

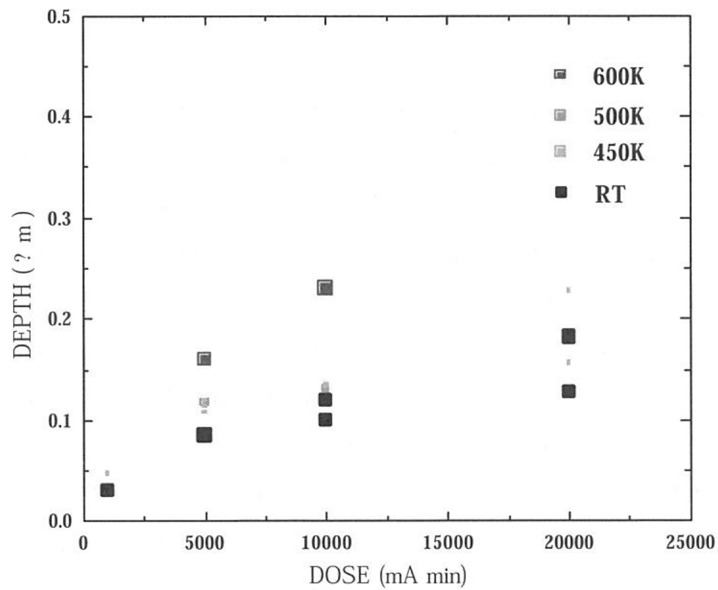


Fig.2 The dependence of the etched depth on the SR dose and the substrate temperature.

(BL4A2)

**3-Dimensional Fine Structure on SOG/Si Surface**

**Fabricated by Focused Ion Beam Mask Patterning and Synchrotron Radiation Etching**

R. Tero [a], H. Okawara [b], K. Nagayama [b] and T. Urisu [a]

[a] Institute for Molecular Science, Myodaiji, Okazaki, 444-8585 Japan

[b] Center for Integrative Bioscience, Myodaiji, Okazaki, 444-8585 Japan

Synchrotron radiation (SR) etching of $SiO_2$ is a unique device process technique [1]. The advantages of SR etching are unique material-selectivity, anisotropicity (vertical side wall) and low contaminations [1, 2]. When $SiO_2$ surfaces are patterned by SR etching using a contact mask [2], spatial resolution is limited by the available size of the photomask. The focused ion beam (FIB) is one of promising techniques which can make nano-scale patterning on metal, insulator and semiconductor materials [3]. Therefore, by applying FIB technique to patterning of etching mask, nano-processing utilizing the advantages of SR etching will become practicable. In this report, we introduce first trial for a new 3-dimensional fine process applying FIB and SR etching methods on spin-on glass (SOG), which is a widely used material in semiconductor processes because planar film with low dielectric constant is easily obtained.

SOG films with thickness of 450-500 nm were obtained after spin-coating on 14 mm square Si wafers followed by curing under flowing $N_2$ ($10^{-3}$ $m^3$/min) at 698 K for 30 min. SR etching was performed in UHV chamber in BL4A2, under mixture of $2.66\times10^{-3}$ Pa of $O_2$ and $6.65\times10^{-2}$ Pa of $SF_6$. Ion beam irradiation was carried out using 31 keV Ga FIB with a beam spot size of ~0.1 $\mu$m.

Figure 1 shows schematic drawings of experimental procedure. First, a SOG film was covered by Co layer with thickness of ~200 nm (Figure 1a). We have reported efficiency of deposited Co film as a SR mask [4]. Then, Co photomask was patterned with FIB (Figure 1b) and the sample was exposed with SR (Figure 1c). At last, Co layer was removed by 0.01 M $HNO_3$ aq (Figure 1d). Figure 2 shows an AFM image of Co layer patterned by FIB. Depth of larger square (5x5 $\mu m^2$) was 95 nm, which meant FIB was stopped in the middle of Co layer. Smaller square (1x1 $\mu m^2$) in the larger one was penetrated the Co layer and arrived to SOG film. Figure 3a shows an AFM image of SOG surface after SR etching ($2.0\times10^4$ mA min) followed by removal of Co layer. 3-dimensional double-step well was successively obtained in single irradiation process. AFM profile in Figure 3b clearly shows that SOG film was removed in the smaller square by direct exposure to SR and Si substrate appeared. In the surrounding 5 nm square region, SOG shrank maybe due to dispersed penetrating light through thin Co layer.

In summary, we have successively demonstrated a new 3-dimensional process on SOG by means of FIB and SR etching. Nanometer scale patterning by this combination method is aimed in the future. Effect of diffusion rate of etching gas and interference of light would also be investigated because these factors possibly become important in nano-scale processing.

## Reference

[1] T. Urisu and H. Kyuragi, J. Vac. Sci. Technol. B **5** (1987) 1436.

[2] H. Akazawa, J. Takahashi, Y. Utsumi, I. Kawashima and T. Urisu, J. Vac. Sci. Technol. A **9** (1991) 2653.

[3] S. Reyntjens and R. Puers, J. Micromech. Microeng. **11** (2001) 287.

[4] C. Wang, Z. Wang, S. More, Y. Nonogaki, S. Yamamura, S. Fujiki, M. Takizawa, T. Urisu, J. Vac. Sci. Technol. B **21**, (2003) 818.

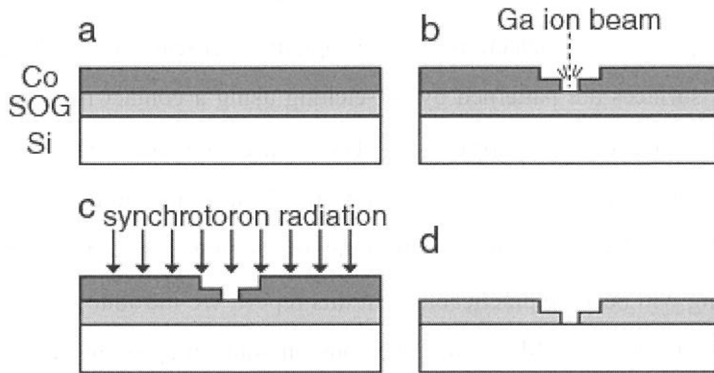


**Figure 1** Schematic drawings of etching procedure on SOG by FIB and SR. Etching gas is $SF_6 + O_2$.

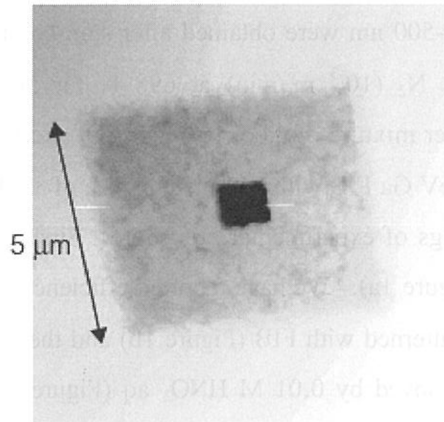


**Figure 2** An AFM image (10x10 ? $m^2$) of Co film on SOG/Si substrate patterned by FIB.

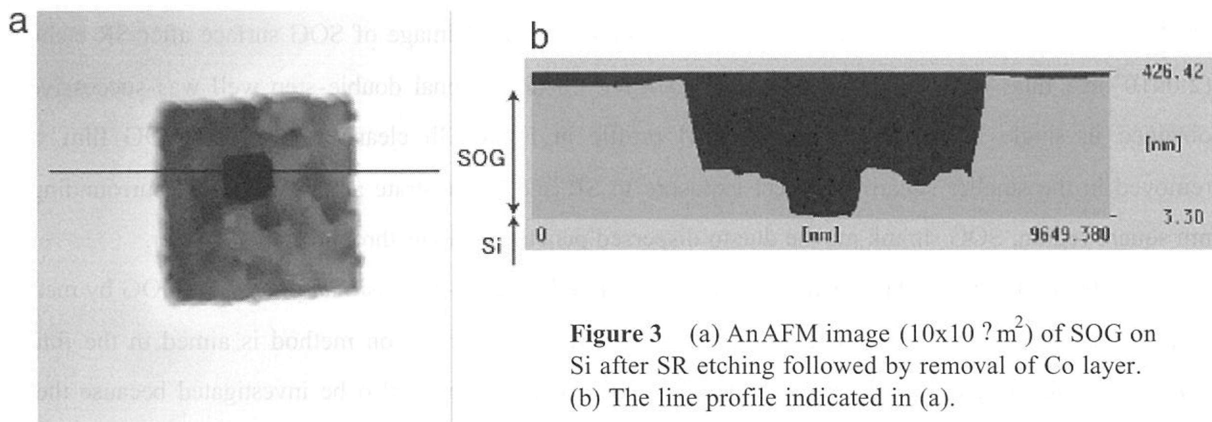


**Figure 3** (a) An AFM image (10x10 ? $m^2$) of SOG on Si after SR etching followed by removal of Co layer. (b) The line profile indicated in (a).

(BL4A2)

# Synchrotron Radiation induced shrinking of Spin-on-glass films and its application to the 3-D microfabrications

Md. Mashiur Rahman[1], Tsuneo Urisu[1,2]

[1] *Institutes for Molecular Science, Myodaiji, Okazaki 444-8585, Japan*
[2] *Department of Structural Molecular Science, The Graduate Univ. for Advanced Studies*

## 1. Introduction

The Spin-on-Glass (SOG), an important material in the semiconductor integrated circuit fabrication, is used to make $SiO_2$ thin films with flat surfaces on the uneven surfaces. Films are typically of a hundreds of nanometers thick. It is usually cured with reducing the thickness by heating to high temperatures (for examples at 400-500°C) in the last stage of the processes[1,2]. In the present work, we have found that the thickness is also reduced by the irradiation of the synchrotron radiation beam with covering the surface by the mask. We are considering that this phenomenon can be applied to three dimensional microfabrications, since the degree of the shrinking depends on the thickness of the mask.

## 2. Experiments

The SOG used in this investigation is a commercial siloxane type SOG (Honeywell, Accuglass312B). The material is then spun on $14mm^2$ silicon wafer at a spin speed of 3000rpm for 10sec. Immediately after spin coating, the film are subjected to three stages of soft bake performed on hot plates at 80°C, 150°C and 250°C for 1 min at each temperature. The final curing is performed at 425°C with a nitrogen gas flow of approximately 1.0 liters/minute. After cure, Spin-on-Glass gives an approximate thickness of 550nm on Si wafer.

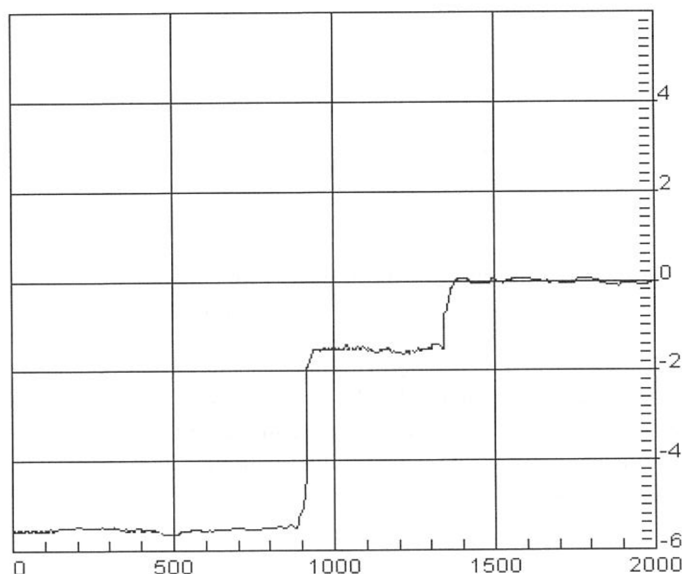


Fig. 1. (a) Step profile of SOG after SR etching after Co mask remove

The synchrotron radiation etching of SOG was conducted using mixture gas of $SF_6$ (0.05 Torr) and $O_2$ (0.002 Torr) at room temperature by using the mask structure. The Co contact mask on SOG surface was fabricated by the deposition of Co thin film (230nm) on a resist pattern made by the photolithography and a lift off technique. A thick 330nm Co mask was deposited with sputtering machine. After 2000mA·hr doze of synchrotron radiation etching, the surface was studied by Dektak step profilometer. Finally the Co mask was removed with 0.01N $HNO_3$ for 3 minutes.

## 3. Result and Discussions

The surface at the open region SOG film was completely etched and the etching was completely stopped on the Si surface[3]. At the region covered only by the thin Co musk (230nm) the thickness of SOG film reduced about 152nm (Fig. 1). At the region covered by thick Co etching mask (560nm), no shrink was observed.

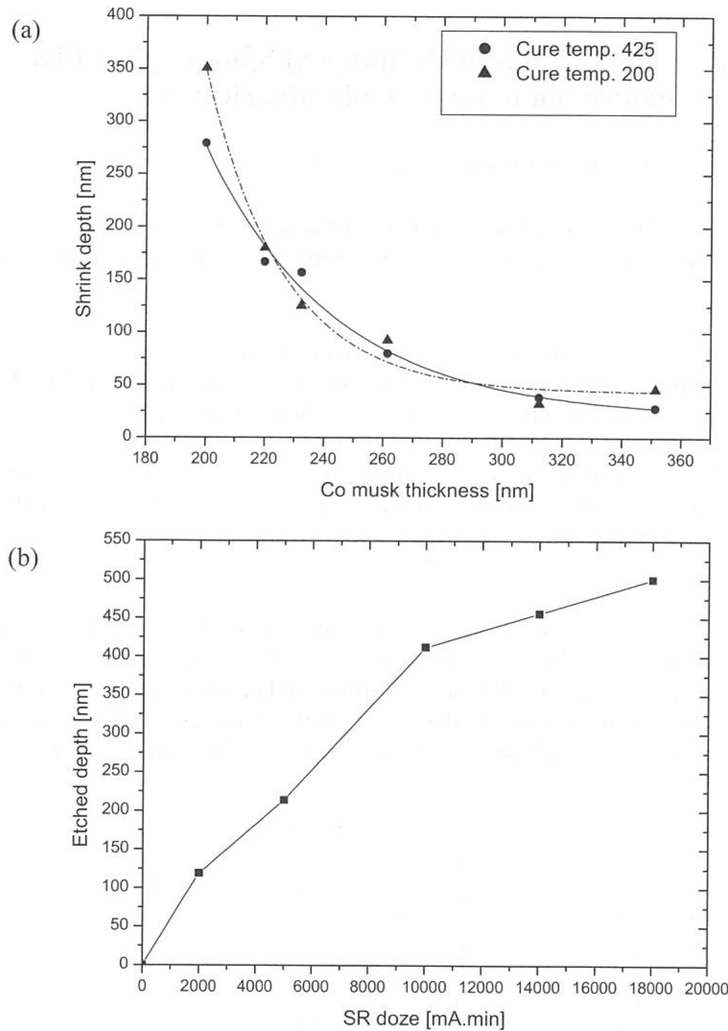


Fig. 2. (a) SR dose dependence of the SOG film etch depth
(b) SOG shrink depth as a function of Co mask thickness

The SR etching rate of SOG was investigated (Fig. 2a) where etched depth of SOG gradually increased with the SR dose. Figure 2(b) shows the SOG shrinkage depth as a function of Co mask thickness. In our experiment we had found that 27% of SOG thickness was reduced with the synchrotron radiation etching with thin Co mask and the SR shrinkage of SOG can be controlled with the Co mask thickness. SR etching can make 3D step pattern by one time of exposure.

## References

[1] J. Taniguchi, K. Kandai, Y. Haruyama and S. Matsui, Jpn. J. Appl. Phys. Vol. 41 (2002) 4304
[2] H. Mizuhara, H. Watanabe, K. Misawa, M. Arimoto, K. Mameno, H. Aoe, H. Hanafusa, K. Yodoshi and M. Akizuki, Applied Surface Science Vol 113-114 (1997) 675
[3] T. Urisu and H. Kyuragi, J. Vac. Sci. Technol. B5, 1436 (1987)

(BL4A2)

# Assignment of surface IR absorption spectra observed in oxidation reactions : $H + H_2O/Si(100)$ and $H_2O + H/Si(100)$

Zhi-Hong Wang[1,2], G. Ranga Rao[2], Tsuneo Urisu[1,2], Shinkoh Nanbu[2], Jun Maki[2], Mutsumi Aoyagi[2,3], Hidekazu Watanabe[4], Kenta Ooi[4]

*[1]The Graduate University for Advanced Studies, [2]IMS, [3]Kyushu University, [4]National Institute of Advanced Industrial Science and Technology*

We have a plan to investigate excitation energy dependence of SR-etching on hydrogen and other chemical compounds adsorbed Si(111) surface by using combination of undulator radiation and STM observations. In this work, infrared reflection absorption spectroscopy using buried metal layer substrates (BML-IRRAS) and density functional cluster calculations are used to analyze the water related oxidation on Si(100)-(2×1) surfaces (2H + $H_2O$/Si(100)-(2×1), 2D + $H_2O$/Si(100)-(2×1) and $H_2O$ + H/Si(100)-(2×1) systems). In addition to the oxygen inserted coupled monohydrides previously reported in 2H + $H_2O$/Si(100)-(2×1) system, three pairs of new doublet bands have been clearly observed for the first time due to the high sensitivity of BML-IRRAS for the perpendicular dynamic dipole moment in the finger print region. Figure 1 shows the observed BML-IRRAS spectra in the reaction system, H + $H_2O$/Si(100)-(2×1) at the H-exposure temperature (Tm) = 373 K for the exposure (D) of 1000 L and 50 L. The curve resolutions assuming a Lorenzian form (solid and dotted lines) are also shown. In these spectra, the negative peaks 823 $cm^{-1}$ and 2082 $cm^{-1}$ are to the stretching vibration modes of Si-H and Si-OH formed by dissociative adsorption of $H_2O$ on the Si(100) surface [1,2], respectively, and the 901 $cm^{-1}$ and 916 $cm^{-1}$ are to the isolated and adjacent scissoring modes of $SiH_2$ ( $\delta\ SiH_{ID}$ and $\delta\ SiH_{AD}$), respectively. We have made the assignment of the observed unknown bands in the following.

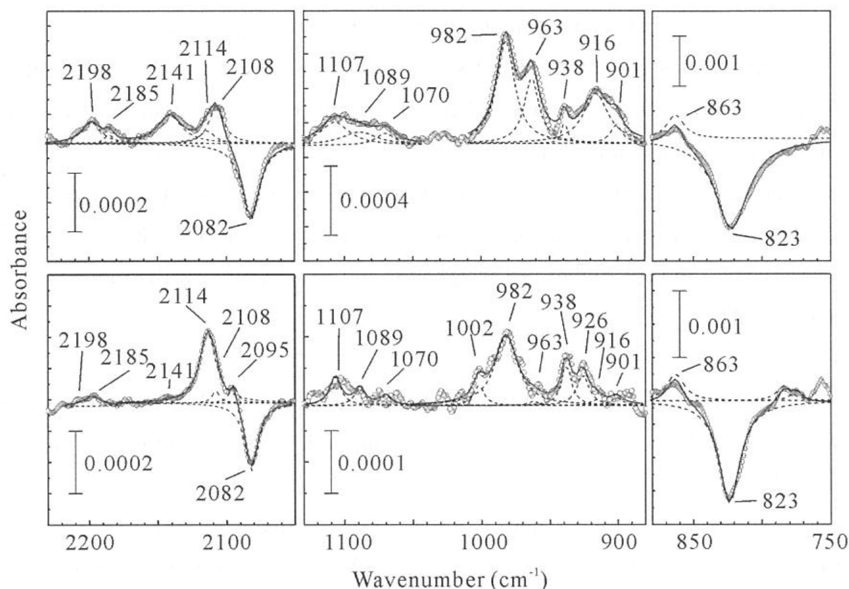


Fig. 1 Observed BML-IRRAS spectrum of the reaction system H + $H_2O$/Si(100)-(2×1) at Tm = 373 K for D = 1000 L (upper) and D = 50 L (lower).

Vibrational frequencies have been calculated using Si9 and Si10 cluster models which including every possible structures from zero to five oxygen insertions to the top silicon layer atoms using B3LYP gradient corrected density functional method with polarized 6-31G** basic set to all atoms. All calculated vibrational frequencies are scaled within each mode type by using the scaling factor which were determined by comparing the assignment-established vibrational frequencies with corresponding calculated frequencies. The frequency

scaling factor (SF) for each vibrational mode has been determined by comparing the reported frequencies, ν $SiH_{CM}$ = 2100 $cm^{-1}$, ν $SiH_{CM(M)}$ = 2118 $cm^{-1}$ and ν $SiO^2{}_{CM(O,M)}$ = 1043 $cm^{-1}$ [2], ν $SiH_{ID}$ = 2090 $cm^{-1}$ and ν $SiH_{AD}$ = 2107 $cm^{-1}$ [3] and our observations δ $SiH_{ID}$ = 901 $cm^{-1}$, and δ $SiH_{AD}$ = 916 $cm^{-1}$ (Fig. 1) with the corresponding calculated one. For all vibrations classified to ν $SiH_{CM}$ type, SF= 0.9538. Similarly, SF=0.9599 for ν $SiH_{CM(M)}$, 0.9532 for ν $SiH_{ID}$, 0.9564 for ν $SiH_{AD}$, 0.9768 for ν SiO, 0.9638 for δ $SiH_{ID}$ (the same value is used for δ $SiH_{CM}$ for simplicity), and 0.98 for δ $SiH_{AD}$.

The definition of symbols used in this report are as follows. ν and δ express the stretching and the scissoring or bending mode, respectively. CM, ID, and AD mean the coupled monohydride , isolated dihydride and adjacent dihydride, respectively. O, OO, and M in the bracket mean the singly and doubly inserted oxygen atoms at the top Si back-bond, and the oxygen atom inserted to the Si-Si dimer bond, respectively. O or OO of the left and the right side of the comma (,) in the bracket mean the left and the right side Si back bond of the Si-Si coupled dimmer or adjacent Si structure, respectively. (O,O) and (O,O') mean the oxygen atoms inserted to the *cis* and *trans* conformations of the Si-Si coupled dimmer or adjacent Si structure back bonds, respectively. The superscripts 1, 2, and 3 mean the different vibration mode expressed by the same symbols.

By comparing Fig. 1 with calculated frequencies, almost all observed unknown bands can be assigned. First, characteristic three pairs of doublet bands, which have been observed by us for the first time [4], are assigned to the scissoring modes of adjacent and isolated $SiH_2$ with zero, one and two inserted back bond oxygen atoms, respectively. The peak at 1002 $cm^{-1}$ is assigned to the overlapping of $\nu$ $SiO_{CM(O)}$ (calc. = 997 $cm^{-1}$) and $\nu$ $SiO^1{}_{CM(O,M)}$ (calc. = 1004 $cm^{-1}$). The 2108 $cm^{-1}$ peak becomes dominant with intensity increase of the three pairs of doublet bands. So it is assigned to the overlapping of $\nu$ $SiH_{ID(O)}$, $\nu$ $SiH_{AD}$ and $\nu$ $SiH_{AD(OO)}$ (symmetric stretching modes of CM oxidized species may overlap). Since the peak intensity of 2114 $cm^{-1}$ shows a similar trend to that of 1002 $cm^{-1}$ peak when increasing the atomic hydrogen dose, it is assigned to the overlapping of the perpendicular components of $\nu$ $SiH_{CM(M)}$ (calc. = 2118 $cm^{-1}$ ) and $\nu$ $SiH^1{}_{CM(O,M)}$ (calc. = 2120 $cm^{-1}$ ). The bands observed in the range from 1070 $cm^{-1}$ to 1107 $cm^{-1}$ are assigned to the overlapping of the SiO stretching of ID and AD with one to four back bond oxygen atoms and of higher oxidized CM species. The bands observed at 2141 $cm^{-1}$ and the higher are assigned to the overlapping of the higher oxidized species of $\nu$ $SiH_{CM}$, $\nu$ $SiH_{ID}$ and $\nu$ $SiH_{AD}$.


(1) M. K. Weldon, B. B. Stefanov, K. Raghavachari, and Y. J. Chabal, Phys. Rev. Lett. **79**, 2851 (1997).

(2) M. K. Weldon, K. T. Queeney, A. B. Gurevich, B. B. Stefanov, Y. J. Chabal, and K. Raghavachari, J. Chem. Phys. **113**, 2440 (2000).

(3) H. Noda and T. Urisu, Chem. Phys. Lett. **326**, 163 (2000).

(4) Z.-H. Wang, T. Urisu, S. Nanbu, J. Maki, M. Aoyagi, H. Watanabe and K. Ooi, being submitted to Phys. Rev. Lett.

(5) Y. J. Chabal and Krishnan Raghavachari, Phys. Rev. Lett. 53, 282 (1984).

(BL4A2)

# Patterning $SiO_2$ Thin Films Using Synchrotron Radiation Stimulated Etching with a Co Contact Mask

C. Wang, S.D. Moré, Z. Wang, S. Yamamura, Y. Nonogaki and T. Urisu

*Department of Vacuum UV Photoscience, Institute for Molecular Science*

Microfabrication technology, a powerful tool in the manufacturing of various types of silicon-based biomedical microdevices, has made a considerable impact on recent biotechnological research. We think that the SR stimulated etching is especially suitable for the mirofabrication of templates for the area-selective deposition of biomaterials, due to its unique features of high spatial resolution, extremely high material selectivity between Si and $SiO_2$, anisotropic etching, low damage, and clean etching atmosphere. In this work, we fabricated the pattern of $SiO_2$ thin films using SR etching with a Co contact mask, and investigate the potential of Co as an etching mask material.

A single-crystal Si (100) wafer covered by native oxide was wet-chemically cleaned and a 200nm $SiO_2$ layer was formed on the cleaned Si surface by 900°C for 12 h in a dry oxygen atmosphere. On the $SiO_2$ surface, a 200nm Co layer was deposited by a sputtering machine and patterned by photolithograph technique. SR etching of the samples was conducted at UVSOR BL4A2. The sample was set normal to the incident SR beam and was irradiated for 8,000mAmin in the reaction gas which is mixture of $SF_6$ (0.05Torr) and $O_2$ (0.002 Torr). After the SR etching, we carried out the area-selective deposition of dodecene on the etched pattern

Figure 1 shows the SR-etched pattern observed by a SEM and a cross-section profile measured by a step profile meter. The $SiO_2$ was effectively etched by the SR radiation with $SF_6 + O_2$ as the reaction gas. The etching took place only in the area irradiated with SR and proceeded in the direction of incident beam and stopped completely on the interface of $SiO_2$/Si. After SR-etching, a thin $SiO_2$ layer covering the etched surface was removed by a dilute HF solution. The dodecene monolayer was coated on this surface by the reaction of dodecene molecules with the hydrogen-terminated Si surface at 200°C. Figure 2 shows the infrared transmission spectrum in the region of CH stretching vibrations measured for the dodecene SAM layer. Combining ellipsometer and water

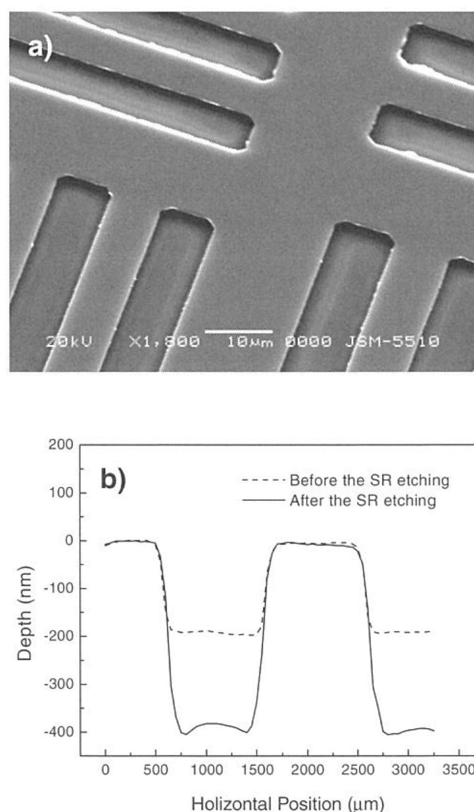


Fig. 1. SEM image of the micropattern after the SR etching with Co mask (a), and the cross-sectional profile of a pattern before and after the SR etcing (b).

contact angle measurements, we conclude that the deposited SAMs were made of alkyl chains in their all-trans conformation, nearly perpendicular to the substrate, and densely packed molecular architecture.

The $SiO_2$ thin film pattern structure was fabricated on the silicon surface by the SR stimulated etching using the $SF_6+O_2$ gas and the Co thin film as the contact mask. The well-ordered SAMs of dodecene were selectively deposited on the etched surface.

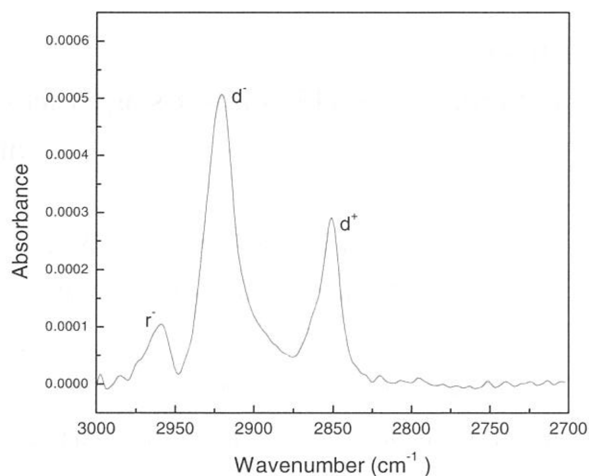


Fig. 2. An infrared spectrum of the dodecene SAM deposited on the SR etched surface. The observaed peaks at $d^+$ ($2850\pm1cm^{-1}$) and $d^-$ ($2918\pm1cm^{-1}$) were assigned to the symmetric and asymmetric stretching vibrations of the methylene ($-CH_2$) groups, respectively, the peak $r^-$ ($2959\pm1cm^{-1}$) was assigned to the asymmetric stretching vibrations of the methyl ($-CH_3$) group.

(BL5A)

# Application of Helical Undulator Radiation for Asymmetric Photochemistry

M. Morita[1], K. Takahashi[2], K. Iseki[1], and A. Hiraya[1]

[1] *Department of Physical Science, Hiroshima University, Higashi-Hiroshima 739-8526*
[2] *UVSOR Facility, Institute for Molecular Science, Okazaki 444-8585*

Study of asymmetric photochemistry needs high intensity circularly polarized UV and VUV light such as Helical Undulator Radiation. Measurements on degree of circular polarization (Pc) of undulator radiation after SGM-TRAIN were carried out prior to the first application of helical undulator at UVSOR for asymmetric photochemistry. Also preliminary measurements of asymmetric photochemistry and asymmetric photo-decomposition of peptide (dl-Ala-dl-Ala) were carried out.

Pc was measured by using UV/VIS polarimeter[1]. Results are shown in Table 1. Fundamental peak of this undulator radiation appeared at 216.5 nm with 45.1 mm gap. Although central wavelength of band-pass-filter (B.P.F.) is deferent from the fundamental peak, $P_c$ at 216.5 and 222 nm are nearly the same. Since the beamline optics for G3 was designed to preserve polarization of undulator radiation at UV and VUV region but those for G1 and G2 was not[2], the Pc after G1 are expected to be smaller than that after G3. However, measured values for G1 and G3 showed opposite trend. Although larger Pc for G1 would occur when the undulator radiation is elliptically polarized (Pc < 0.8) with elongated in vertical direction (prolate ellipse), it seems unlikely that the Pc of the helical undulator is below 0.9 and prolate. Another possible reason of smaller Pc value for G3 is misalignment of optics for G3 that undulator axis and monochromator axis for G3 dose not coincide. This possibility is also supported by the fact that the observed intensity is $10^{-2}$ times weaker for G3. This large reduction in intensity in the present photon energy cannot be explained by reflection loss at the normal incidence optics. Therefore the reason of the small Pc for G3 is thought to be the misalignment of G3 optics.

Table 1. Results of measurements at 45.1 mm gap Left-handed mode with S1 and S2 of 1 mm.

| Grating/order | Wavelength | $P_C$ |
|---|---|---|
| G1(grazing)/0th | 222 nm (B.P.F.) | 0.87 ± 0.08 |
| G3(normal)/0th | 222 nm (B.P.F.) | 0.75 ± 0.10 |
| G3(normal)/1st | 216.5 nm | 0.70 ± 0.10 |

In this measurement, it was found that the sense of polarization defined at UVSOR (See manual of BL5A) had been opposite. The sense of rotation of circularly (elliptically) polarized radiation is reversed by normal incident optics (mirror and grating). On the other hand, grazing incident optics *do not* reverse the sense of polarization but only change (increase or decrease) the orientation angle defined between major axis of polarization ellipse and horizontal axis. Although the monochromator at BL5A has two optical configurations, normal incident (G3) and grazing incident (G1, G2), the sense of polarization after pre-focusing mirror(s) will be conserved for both configurations. In the grazing incident configuration, the sense of rotation is not reversed because of no normal incident optics, only the orientation angle of the polarization ellipse is changed. In the normal incident configuration, two times reversals of the sense of polarization at the incident mirror and the incident grating (G3) result in the same sense of polarization after the monochromator.

Asymmetric photodecomposition experiment of dl-Ala-dl-Ala peptide (CD value/UV value ~ 0.004) was performed with 45 mm gap (fundamental peak at 222 nm) with using G1 grating. G1 was selected because intensity and Pc of G1 were larger than those of G3. First CD band of l-Ala-l-Ala is appeared at about 225 nm. After irradiation of 9 hours each for left- and right-handed circularly polarized radiation, both irradiation samples were analyzed by using High Performance Liquid Chromatography (HPLC) in our laboratory. It was found that too little peptide was decomposed to detect asymmetric decomposition of l-Ala-l-Ala and d-Ala-d-Ala enantiomer. The reason of this result will be that either this peptide has small UV absorbance (~100 $M^{-1}cm^{-1}$) or is not easily decomposed in this photon energy used, or both.

**References**

[1] G. V. Rybalchenko et al, Problems of Atomic Science and Technology, **1** (2001) 102
[2] M. Kamada et al, Rev. Sci. Instrum., **66** (1995) 1537

(BL5A)

# Core-level photoemission spectroscopy of Mg or/and Li atoms adsorbed on Cu(001)

Mingshu CHEN, Hiroshi TOCHIHARA, and Kazutoshi TAKAHASHI *

*Department of Molecular and Material Sciences, Interdisciplinary Graduate School of Engineering Sciences, Kyushu University, Fukuoka 816-8580*
** UVSOR Facility, Institute for Molecular Science, Okazaki 444-8585*

We have recently studied surface structures formed on Cu(001) by the coadsorption of Li and Mg atoms at room temperature (RT) by low-energy electron diffraction (LEED) analysis [1]. In the individual adsorption of Li, the missing-row type restructuring took place and a (2x1) structure was completed at Li coverage 0.4 [1], while a c(2x2) substitutional structure was formed for Mg at coverage 0.5 [2]. In the coadsorption of Li and Mg, a $(2\sqrt{2} \times \sqrt{2})$R45° structure was formed at both coverages 0.25, and its structure was determined by LEED analysis as shown in Fig. 1(a) [3]. Furthermore, its formation process was also studied by LEED.

In this study we have measured core-level photoemission spectroscopy of Li 1s and Mg 2p both in the individual adsorption and in the coadsorption to clarify electronic properties of these surface structures and to confirm the formation process of the $(2\sqrt{2} \times \sqrt{2})$R45° structure .

The experiments were performed at beamline 5A. The pressure during measurements was about $1\times10^{-10}$ Torr. Mg and Li atoms were evaporated onto the Cu(001) surface from a Knudsen cell and a SAES getter, respectively. The coverages were calibrated by LEED patterns of the c(2x2)-Mg [2] and (2x1)-Li [1] structures at RT. The contamination and the $H_2O$ adsorption were checked by AES spectroscopy after the measurements. The binding energy was determined from the Fermi edge of the clean Cu(001) surface.

Mg 2p and Li 1s core-level spectra in the individual adsorption of Mg and Li at RT are shown in Fig. 1(b) and 1(c), respectively. [For comparison, Li 1s spectra at about 150 K are shown in Fig. 1(d).] Both spectra show similar changes: at low coverages the peak position is constant, then shifts to lower binding energy at full monolayer coverages, and shifts back to higher binding energy at higher coverages where bulk-like alloys start to form. These results are consistent with the structure changes in the individual adsorptions.

The coadsorption of Mg and Li on Cu(001) at RT was carried out at two adsorption sequences, Li+Mg and Mg+Li, as shown in Fig. 1(e) and (f). In the former sequence, Mg atoms are deposited on Li pre-adsorbed surfaces, Mg deposition at coverages less 0.1 do not have obvious effect on the Li 1s binding energy, since Mg atoms are located at regions free of Li. Upon further deposition of Mg, the Li 1s peak continuously shifts to higher binding energy, due to the formation of the $(2\sqrt{2} \times \sqrt{2})$R45°-Mg,Li structure. This shift may be attributed to the electron transfer from Li to Mg. In fact, the Mg 2p peak shifts to lower binding energy. In the opposite order of deposition, i.e. Mg first then Li, the Mg 2p peak also shifts to lower binding energy due to the presence of Li atoms, and the Li 1s peak at low coverages shows higher binding energy. This result is consistent with that obtained in the opposite order of adsorption: the same direction of the charge donation.

In short, we have measured the core-level photoemission spectra of Li 1s and Mg 2p from the Cu(001) surface coadsorbed by Mg and Li as well as from individual adsorption of Li or Mg . Good correlation was found between electronic properties of adsorbates and surface structures.

References

[1] H. Tochihara, S. Mizuno, Prog. Surf. Sci. 58 (1998) 1.
[2] M.S. Chen et al., Surf. Sci. 470 (2000) 53.
[3] M.S. Chen, S. Mizuno, H. Tochihara, Surf. Sci. 493 (2001) 91.

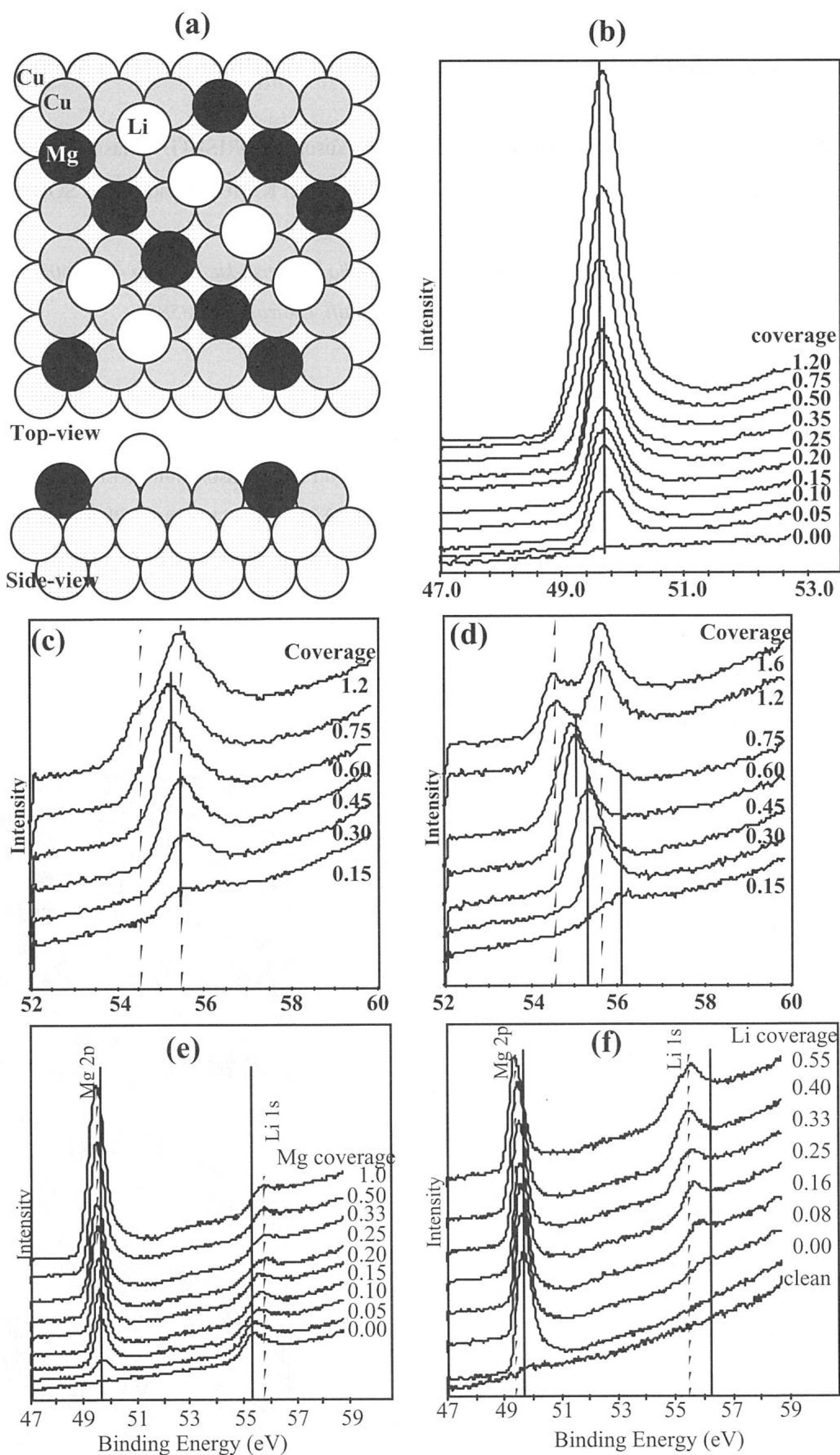


**Figure (a) Top and side views of the Cu(001)-(2√2x√2)R45°-Mg,Li structure. (b)-(f) Photo emission spectra: (b) Mg 2p peak of Mg adsorption on Cu(001) at room temperature (RT); (c) and (d) Li 1s peaks of adsorption Li on Cu(001) at room and low temperature respectively; (e) and (f) Mg 2p and Li 1s photoelectron spectra of (e) the adsorption of Mg on Li pre-adsorption surface (θLi=0.25) and (f) of Li on Mg pre-adsorption surface (θMg=0.25) on Cu(001) at RT.**

(BL5A)

# Sn 4*d*, Pb 5*d* and Si 2*p* Core-level Photoemission Study of (Pb,Sn)/Si(111) Surface

Kurando SHIMBA, Tatsunori MIZUTANI, Hiroko MURAYAMA, Yusuke MORISHITA, Masahiko KATO, Shinya YAGI, Junji YUHARA, *†Kazutoshi TAKAHASHI, *Shin-ichi KIMURA and Kazuo SODA

*Graduate School of Engineering, Nagoya University, Furo-cho, Chikusa-ku, Nagoya 464-8603*
**UVSOR, Institute for Molecular Science, Myodaiji, Okazaki 444-8585*

Binary adsorbate system on a semiconductor surface has a possibility of showing unique surface atomic arrangement and electronic structure and hence related fascinating properties, which are different from those of single adsorbate system [1]. Recently, we have found new surfaces on the coadsorption of Pb and Sn on the Si(111) surface by using scanning tunneling microscopy (STM) [2,3]: Si(111) √7x√3-(Pb,Sn) surface at coverage of 0.4 ML Pb and 0.4 ML Sn, and Si(111) 2√7x3-(Pb,Sn) surface at those of 0.25 ML Pb and 0.5 ML Sn. Here, 1 ML is defined as $7.8 \times 10^{14}$ atms/cm$^2$. Their STM images are shown in Fig.1 for a filled state and scan size of 5x5 nm$^2$. However, detailed atomic arrangements for these surfaces have not been clarified yet. Thus, we have measured the Pb 5*d*, Sn 4*d* and Si 2*p* photoelectron spectra of these surfaces in order to study their bonding properties and adsorbing sites.

The Si(111) √7x√3-(Pb,Sn) surface was prepared on a substrate of an n-type Si(111) wafer of 5 Ωcm in a size of 5x10x0.5 mm$^3$ by annealing at 620 K after deposition about 1 ML Pb onto the Si(111) √3x√3 + faint 2√3x2√3-Sn surface with the coverage of 0.4 ML, which was made by deposition of 1 ML Sn onto the clean Si(111)7x7 surface and subsequent annealing at 970 K. The Si(111) 2√7x3 -(Pb,Sn) surface was prepared on the Si substrate by annealing at 620 K after deposition about 1 ML Pb onto the Si(111) √3x√3 + faint 2√3x2√3-Sn surface with the coverage of 0.5 ML which was made by the same method as the preparation of the Si √7x√3 -(Pb,Sn) surface. Photoelectron measurement was performed at about 100 K. The origin of the binding energy was determined from the Fermi edge of an evaporated Au film which was electrically connected to the Si substrate. Total energy resolution $\Delta E$ were set to about 160 meV for the excitation photon energy $h\nu$ = 52 eV, and $\Delta E \approx$ 180 meV for $h\nu$= 110 eV and 130 eV.

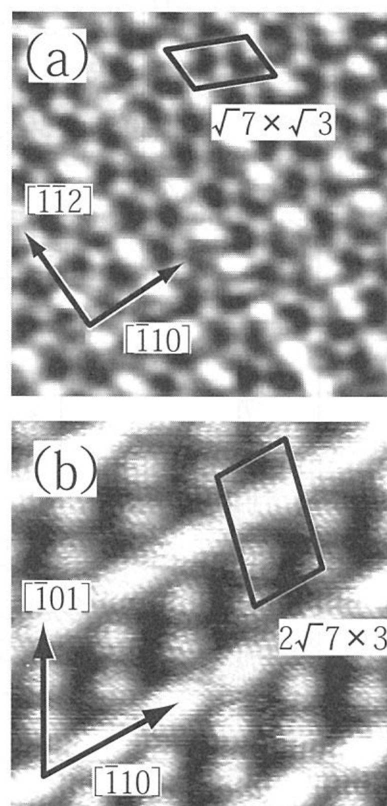


Fig.1 Filled state STM images of (a) Si(111) √7x√3-(Pb,Sn) and (b) Si(111) 2√7x3-(Pb,Sn) surfaces.

The Sn 4*d* and Pb 5*d* photoelectron spectra are shown in Fig.2 in comparison with the single adsorbate system of the Si(111) √3x√3-Sn or Pb. Both the Sn4*d* spectra for the Si(111) √7x√3-(Pb,Sn) and Si(111) 2√7x3-(Pb,Sn) surfaces consist of two components. Although only one Pb 5*d* component was observed at room

temperature for the Si(111) √7x√3-(Pb,Sn) surface in the previous study [4], the present low temperature Pb 5*d* spectrum shows two components. The Pb 5*d* spectrum for the Si(111) 2√7x3-(Pb,Sn) surface has single component.

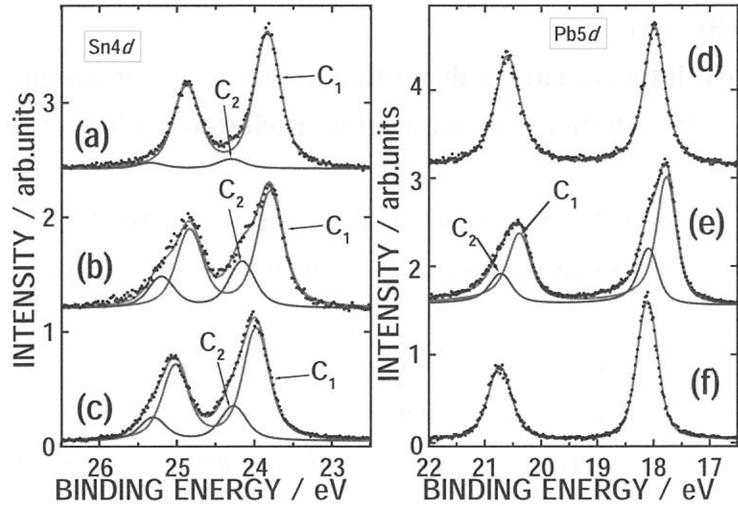


Fig.2 Sn4*d* and Pd5*d* photoelectron spectra of Si(111) √3 × √3-Sn surface with 1/6 ML Sn (a), Si(111) √3 × √3-Pb surface with 1/6 ML Pb (d), Si(111) √7 × √3-(Pb,Sn) surface (b)(e), and Si(111) 2√7 × 3-(Pb,Sn) surface (c)(f).

The results of the Si 2*p* core-level spectra of Si(111) 2√7x3-(Pb,Sn) and Si(111) √7x√3-(Pb,Sn) surfaces are summarized in Figs.3 and 4. These spectra can be decomposed into a bulk component B and three surface components $S_1$~$S_3$ for the Si(111) 2√7x3-(Pb,Sn) surface, and into a bulk component B and four surface components $S_1$~$S_4$ for the Si(111) √7x√3-(Pb,Sn) surface.

Thus, the present study shows that there are at least two Sn and one Pb adsorbing sites on the Si(111) 2√7x3-(Pb,Sn) surface at low temperature and at least two Sn and two Pb adsorbing sites on the Si(111) √7x√3-(Pb,Sn) surface.

† Present address: Synchrotron Light Application Research Center, Saga University, Honjou 1, Saga 840-9502.


[1] J.Yuhara, R.Ishigami, K.Morita, Surf. Sci. **326** (1995) 133.

[2] J.Yuhara, D.Nakamura, K.Soda and K.Morita, Surf. Sci. **482-485** (2001) 1374.

[3] J.Yuhara, S.Yuasa, O.Yoshimoto, D.Nakamura, K.Soda and M.Kamada, Nucl. Instrum. & Meth. in Phys. Res. B **199** (2003) 422.

[4] K.Soda, J.Yuhara, T.Takada, O.Yoshimoto, M.Kato, S.Yagi, K.Morita and M.Kamada, *ibid.* **199** (2003) 416.


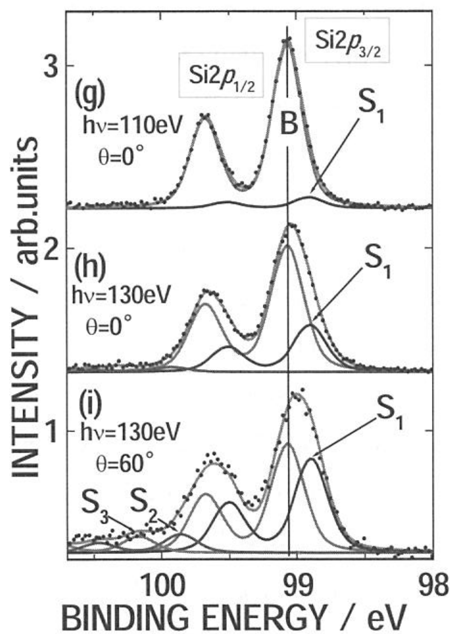


Fig.3 Si 2*p* spectra of Si(111)2√7 × 3-(Pb,Sn) surface.

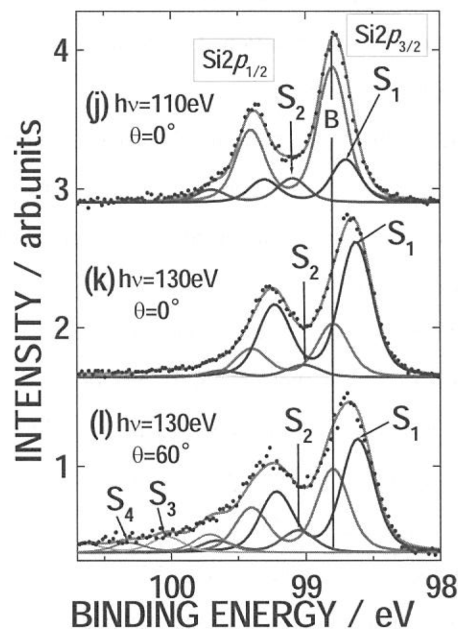


Fig.4 Si 2*p* spectra of Si(111) √7 × √3-(Pb,Sn) surface.

(BL-5B)

# Evolution of energy deposition processes in anthracene single crystal from photochemistry to radiation chemistry under excitation with synchrotron radiation from 3 to 700 eV

Yasuyuki Miyake [A)], Madoka Ueno [A)], Jin Zhaohui [B)], Masahito Tanaka [B)], Fusae Kaneko [A)], Atushi Kasahara [C)], Kazumichi Nakagawa [C)], Hironobu Nishimagi [D)], Hiroyuki Kobayashi [D)] and Masahiro Kotani [D)]

[A)] *Graduate School of Cultural Studies and Human Sciences, Kobe University, Tsurukabuto, Rokkodai, Nada-Ku, Kobe 657-8501.*

[B)] *Graduate school of Science and Technology, Kobe University, Tsurukabuto Tsurukabuto, Nada-Ku, Kobe 657-8501.*

[C)] *Faculty of Human Development, Kobe University, Tsurukabuto, Nada-Ku, Kobe 657-8501, nakagawa@kobe-u.ac.jp.*

[D)] *Faculty of Science, Gakushuin University, Mejiro, Tokyo 171-8588.*

In the case of photochemical reaction, yield Y is well known to be essentially controlled by resonance ($Y=\delta(h\nu-E)$), while in the case of radiation chemistry the reaction yield is nearly proportional to the incident photon energy ($Y\propto h\nu$) due to increase of secondary electrons. In the latter case, reaction occurs in nonhomogeneous way inside of the high density excited area called as "spur". We measured absolute values of quantum yield $\Phi$ of singlet exciton ($S_1$) formation as a function of incident photon energy $h\nu$ in anthracene single crystals in an attempt to explore the boundary between photochemistry effect and radiation chemistry effect. We also measured the fluorescence time decay curves in order to study the minimum energy of spur formation.

Anthracene single crystals with thickness of about 0.2 mm were grown by sublimation method from scintillation grade anthracene powder after purification by zone melting method. Experiments were performed at BL-5B. Samples were placed in the vacuum chamber of which pressure was about $10^{-8}$ torr and were cooled at 200 K to avoid evaporation. The quantum yield $\Phi$ was defined to be $\Phi(h\nu) = N^{S1}(h\nu) / N^{SR}(h\nu)$, where $N^{S1}(h\nu)$ is the number of singlet excitons produced by SR of which photon energy is $h\nu$ and $N^{SR}(h\nu)$ is the incident photon number of $h\nu$. Magnitude of $N^{SR}(h\nu)$ was determined by the drain current from the Au film freshly evaporated in vacuum on the basis of photoelectron yield data by Henke et al.. $N^{S1}(h\nu)$ was determined by comparing the $S_1$ fluorescence intensity due to SR excitation with that due to mercury lamp (3.4 eV) excitation. For the latter case $\Phi$ (3.4 eV) was reported to be be 0.81 [1]. The measurement of fluorescence time decay was carried out under the single bunch mode operation. The time-correlated single-photon counting technique was used.

Fig. 1 shows the quantum yield $\Phi$ spectra of anthracene for $3 \leq h\nu \leq 700$ eV excitation, in which data by Kishigami et al. [2] obtained at KEK-PF and Horiuchi et al. [3] obtained at UVSOR are included. As seen from the figure, above 75 eV , except for the carbon K-edge region, values of $\Phi$ were found to increase linearly as a function of photon energy $h\nu$. On the basis of this linear relation of $\Phi$ with $h\nu$, we concluded that the radiation chemistry effect becomes dominant above 75 eV. As shown in Fig. 2, in the 20 ~ 40 eV region, the $\Phi$ shows a wealth of structures and is not linear to incident photon energy. These structures have no clear correspondence with the EELS

spectrum of anthracene by H. Venghaus et al. [4]. The magnitude of Φ is about 1.2, which is not so larger than the value 0.81 induced by 3.4 eV. It may indicate that although some resonant electronic states are responsible to production of $S_1$ excitons, there are strong contribution of non-radiative decay processes. On the basis of this implication of resonance states, we concluded that ,below 40 eV, photochemistry effect seems to be dominant.

Fig. 3 shows the $S_1$ fluorescence decay curve obtained under excitation at 6.2 eV, 100 eV, 150 eV, 200 eV and 250 eV. It is natural to consider that the 6.2 eV photons cannot produce spur. We carefully examined the appearance of short-lived fluorescence decay ("spike") due to strong quenching by electrons, holes and radical species inside of spur. As seen from the Fig.3, we cannot observe any short-lived spikes. Through a calculation of diffusion length L of electron and holes in 1 ns from excitation (L>57 nm), we concluded that the spur diffused away already in the time scale of nanosecond. Formation and decay of spur may be observed via femto-second SR. This is a very challenging project in future.

References: [1] J. Tatezaki et al., to be published. [2] Y. Kishigami, master thesis, Kobe University, (2000).
[3] H. Horiuchi et al., UVSOR Activity Report (1996) 218. [4] H. Venghaus, Z. Physik, 239, (1970) 289.

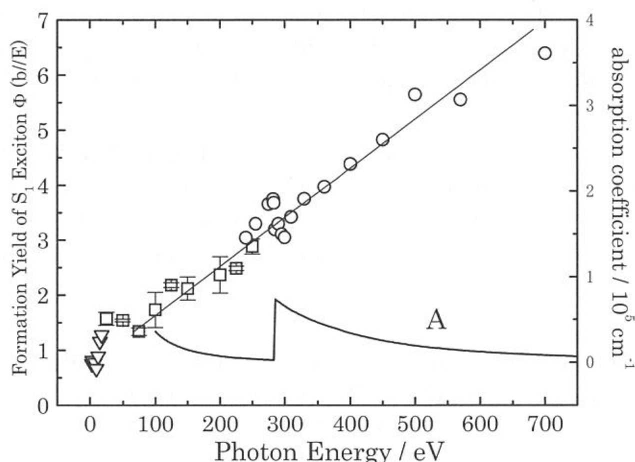


Fig.1. Absorption spectrum (curve A) :
Quantum yield of $S_1$ exciton in anthracene single crystal. O: [2], ∇: [3].

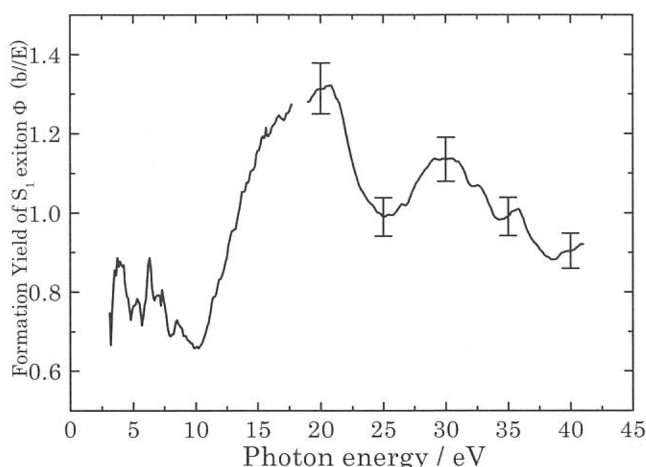


Fig.2 Quantum yield of $S_1$ exciton in anthracene single crystal in 3 ~ 40 eV. 3 ~ 20 eV[3].

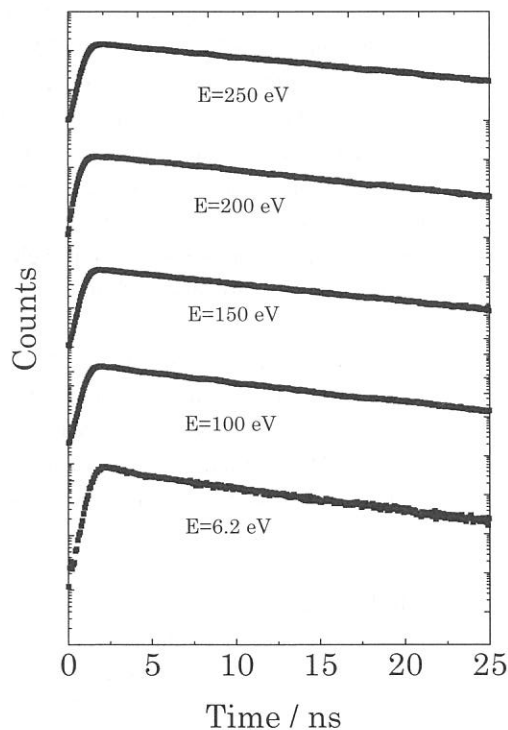


Fig. 3 Fluorescence time decay curves.

**(BL5B)**

# Electron and Photon Stimulated Desorption of $(H_2O)_nH^+$ from Water Adsorbed on Rare Gas Solids

T. Tachibana[1], Y. Yamauchi[1], H. Nagasaki[1], T. Hirayama[2], T. Miura[1], M. Sakurai[3] and I. Arakawa[1]

*1) Dept. Phys., Gakushuin Univ., Mejiro, Tosima, Tokyo 171-8588, Japan*
*2) Dept. Phys., Rikkyo Univ., Nisiikebukuro, Tokyo 171-8501, Japan*
*3) Dept. Phys., Kobe Univ., Rokkodai, Nada, Kobe 657-8501, Japan*

There has been a growing interest in the properties of ice surface and ice particle for both fundamental and practical points of view in the field of the surface, environmental and the planetary sciences. We have studied electron stimulated desorption (ESD) and photon stimulated desorption (PSD) of ions from water adsorbed on a rare gas solid (RGS). In a time-of-flight (TOF) mass spectrum, a series of ionized clusters are observed, which were thought to be protonated water clusters[1]. In the present study, we have investigated the cluster size distribution and the desorption yield for dependence on a water film thickness and for excitation energy.

The experiments have been carried out in two independent ultra-high vacuum systems; one for ESD at the Gakushuin University and the other for PSD at the beam line 5B at UVSOR in Institute for Molecular Science, Okazaki. A TOF technique was applied for the mass analysis of desorbed ions both ESD and PSD experiments.

The ESD chamber is equipped with a He gas flow cryostat, TOF detector, and a pulsed electron gun. Water was adsorbed on the Kr or Xe film which was condensed on a Cu substrate attached to the He gas flow cryostat.The substrate was held at 30K.

In UVSOR, a liquid He cryostat is installed in an UHV chamber. Ar was condensed on a Pt substrate at temperature of 6K or lower. Monochromatized synchrotron radiation in the range 2.0-240nm was focused on the sample. The incident angle of the photon beam was 30 deg from the normal direction of the sample surface. The desorption yield was normalized by the light intensity, which was continuously monitored by the photoelectronic current from a gold-plated mesh, inserted in the beam line.

The ESD-TOF experiments of $H_2O$/Xe and $H_2O$/Kr is shown in Fig. 1. The distribution of n shows the strong dependence on the amount of water condensed. This results agree with ESD experiment on $D_2O$/Ar [2]. At the film of average thickness less than 1ML, the cluster ions with the size n up to 17 were observed. The cluster size distribution differs with RGS substrates used.

The results of PSD experiment of $H_2O$/Ar is shown in Fig. 2, in which the series of $(H_2O)_nH^+$ {n=1-9} was observed. The excitation energy dependence of the cluster yield is shown in Fig. 3. The threshold for the desorption of the cluster ions was found at 240eV. The desorption yield dependence on the incident energy after the threshold is clearly corresponds to the absorption spectrum of solid Ar near the onset of 2p transitions[3]. The dependence on the desorption yield of a incident photon energy indicated that the core excitation of rare gas atoms leads the desorption of cluster ions.

We have observed ESD and PSD ions from water adsorbed on RGSs. In both cases, protonated water clusters were observed. We can conclude from the thickness dependence that the cluster ions are originated from the isolated water clusters, which already exist on a surface of RGS, but not from the surface of bulk solid ice.

The PSD result indicates that charge exchange, intermolecular Auger decay for example, between Ar and $H_2O$ is likely to plays an important role in the desorption mechanism [4] .

References

[1] T. Matsuo, T. Tonuma, H. Kumagai, H. Shibata and Tawara, J. Chem. Phys. **101** (1994) 5356
[2] R. Souda, Surf. Sci. **511,** 147 (2002)
[3] Hansel at al., J. Phys. **32,** 236 (1971)
[4] A. Hoshino, T. Hirayama and I. Arakawa, Appl. Surf. Sci. **70,** 308 (1993)

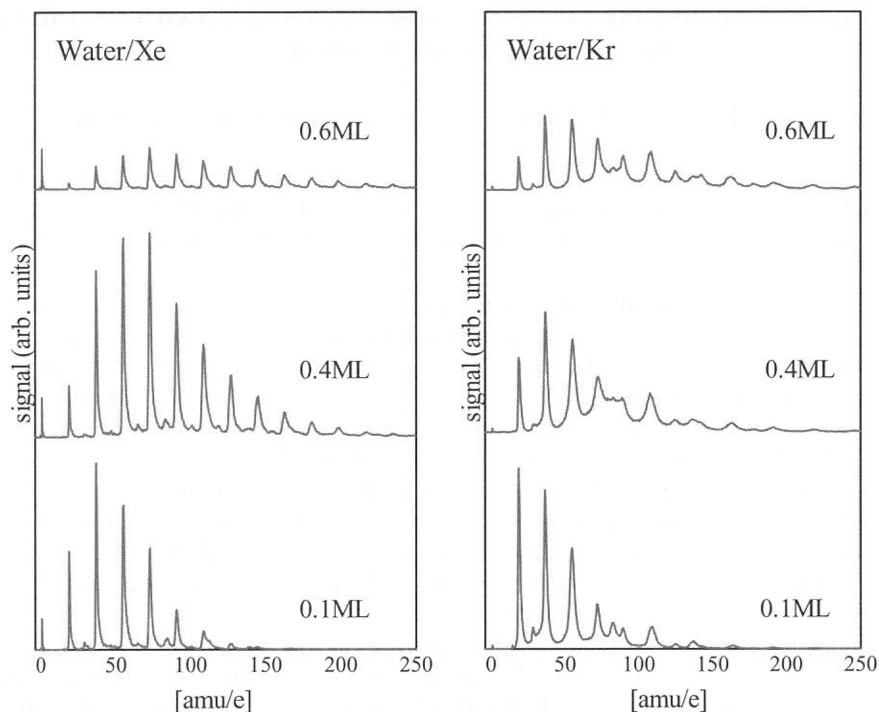


*Fig. 1: Mass spectrum of ESD ions from water on Xe and Kr, and these dependence on thickness of a water film. The samples irradiated with 450eV pulsed electron beam.*

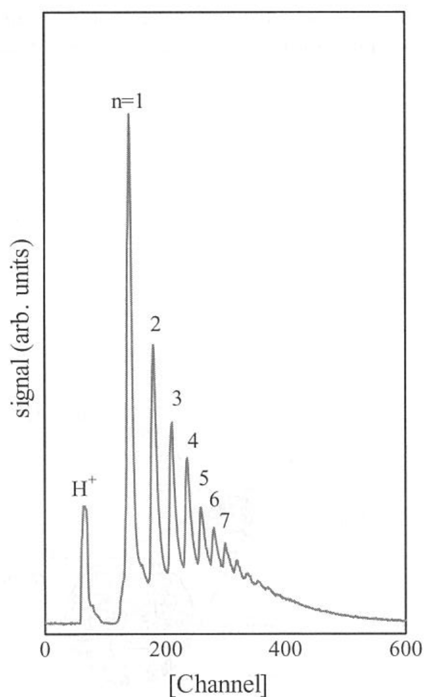


*Fig. 1: Mass spectrum of ESD ions from water on Xe and Kr, and these dependence on thickness of a water*

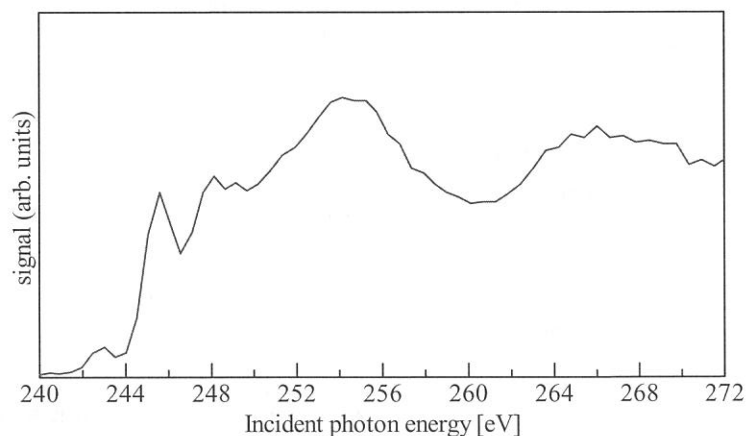


*Fig. 3: Excitation energy dependence of the PSD cluster ions(n=1-7)yield from water adsorbed on solid Ar.*

(BL7U)

# Design of Undulator Beam Line for in-situ Observation of Synchrotron Radiation Stimulated Etching by STM

Y. Nonogaki[A], M. Kato[B], E. Shigemasa[B], K. Matsushita[C], M. Suzui[C] and T. Urisu[A]

[A]*Department of Vacuum UV Photoscience, Institute for Molecular Science, Myodaiji, Okazaki 444-8585, Japan*
[B]*UVSOR Faclity, Institute for Molecular Science, Myodaiji, Okazaki, 444-8585, Japan.*
[C]*Equipment Development Center, Institute for Molecular Science, Myodaiji, Okazaki, 444-8585, Japan*

Concerning the synchrotron radiation (SR) stimulated photochemical processes, the importance of the excitation energy dependence has been the common understanding among the research community, since the first demonstration of SR etching in 1987[1]. The most difficult point of this observation has been in the fact that the large photon density (~$10^{20}$/cm$^2$) is required to induce an observable amount of the reaction. The first in-situ STM observation of the SR stimulated etching has been reported by T. Miyamae et al. using bending magnet beam line, in which nonmonochromatised (white) beam was used to get large photon density[2]. We think that combination of undulator radiation and STM observations enables the measurement of excitation energy dependence of photochemical reactions, because undulator has a quasi-monochromatised beam in high intensity, and because STM requires only a small area for observations, and has high sensitivity for the small changes on surface morphology. Based on these concept, we have designed the undulator beam line specialized for the in-situ observation of SR etching and are now constructing it.

The schematic drawings of the BL7U and the STM apparatus are shown in Fig. 1 and 2, respectively. The undulator equipped with BL7U is in-vacuum type, of which period length is 36mm and number of periods is 26. The first order radiation will be tuned from 70eV to 140eV. Due to achievement of high photon flux density, the beam line has no monochromator and has two cylindrical mirrors for vertical and horizontal focusing. The first mirror set at incident angle of 86° and can move by ±15mm across the optical path for branching the beam line. Incident angle of the second mirror is 87° and this mirror can move along three axes for adjusting spot position on the sample surface. These two mirrors suppress the higher order radiation from the undulator into ~10% with respect to the 1st order radiation. This optics provide a 0.20mm x1.3mm (FWHM) spot on sample surface with photon density of $10^{23}$ cm$^{-2}$ (at 100eV) for 1hour exposure. The STM system is designed so that surface is observed without sample transfer after irradiation.

We plan to investigate excitation energy dependece of SR-etching on surface oxide of Si (111) surfaces and on hydrogen adsorbed Si (111) surfaces by using combination of undulator radiation and STM observations.

## References

[1] T. Urisu et al., J. Vac. Sci. Technol. B 5 1436 (1987).
[2] T. Miyamae et al., J. Vac. Sci. Technol. A 17 1733 (1999).

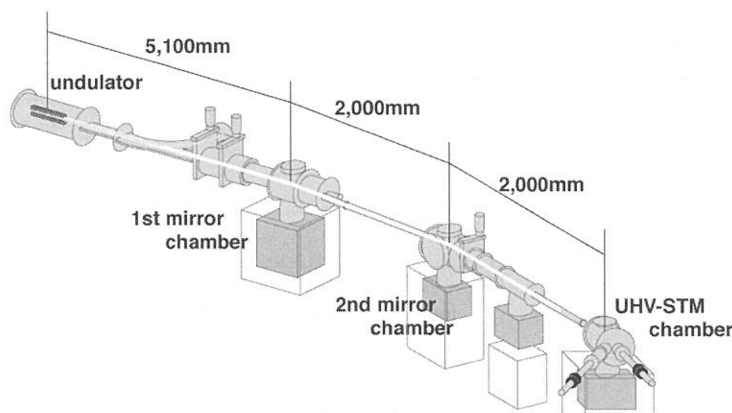


Fig. 1. Schematic drawing of BL7U at UVSOR.

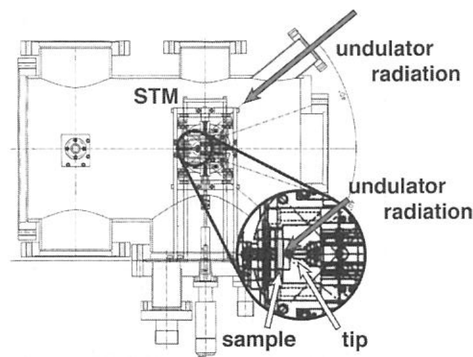


Fig. 2. Plan view of STM chamber. Incident angle of undulator radiation is 40° with respect to sample surface.

(BL8A)

# Formation of Carbon Structure Using Synchrotron Radiation Irradiation

Takayuki Ohta, Hisao Nagai, Masaru Hori and Toshio Goto,
*Mineo Hiramatsu

*Department of Quantum Engineering, Nagoya University,*
*Chikusa-ku, Nagoya, 464-8603*
**Department of Electrical and Electronic Engineering, Meijo University,*
*Tempaku-ku, Nagoya, 468-8502*

## INTRODUCTION

Electron field emission from various carbon materials has recently attracted much attention for their promising applications in displays and other microelectronic devices. Diamond, nanodiamond, diamond-like carbon and carbon nanotube are widely investigated and demonstrated to initiate emission at reasonably low fields. Among them, carbon materials such as nanodiamond, diamond-like carbon and carbon nanotube exhibit conspicuously excellent field emission characteristics, including very low threshold electrical fields, large emission current density, and high emission site density.

Previously, we demonstrated the anisotropic micromachining and film formation of Teflon (fluorocarbon polymer) using synchrotron radiation (SR) ablation process [1, 2]. Moreover, in order to clarify the mechanism of SR ablation, we have performed polytetrafluoroethylene (PTFE) micromachining by selecting the photon energy distribution of incident SR beam with carbon (C) membrane and carbon/magnesium fluoride / carbon (C / $MgF_x$ / C) triple-layered membrane as filters. From these results, the photons with energies below 120 eV were found to contribute to the ablation of PTFE [3]. In addition, SR ablation was applied to the pattern formation of metal fluoride films [4], and the deposition of carbon films [5].

It is reported that the carbon nanotube [6], nano-diamond film [7] and fullerene [8] were formed by camphor ($C_6H_{10}O$). In this report, the material processing using the SR induced reaction was applied to the deposition of carbon structure using camphor as a material. In this study, at the preliminary experiment of carbon structure from the camphor, the deposition was demonstrated using SR irradiation.

## EXPERIMENT

The experiments were performed at a beam line BL-8A of UVSOR. Figure 1 shows a schematic diagram of the apparatus used in this study. It consisted of the SR beam, a reaction chamber, and a pumping system. The reaction chamber was evacuated to $1 \times 10^{-5}$ Torr using a turbomolecular pump before irradiation by the SR beam. The carbon structure was formed by camphor. Figure 2 shows the structure of camphor. The pressure was kept at 100 mTorr in the reaction chamber. As the substrate, Si evaporated with Ni was used. The substrate was set perpendicular to the SR beam. The sample was heated by using Tungsten filament. Tungsten filament was set on the front of the substrate at the distance of 2cm.The sample temperature was monitored with a thermocouple in contact with the surface of sample.

## RESULTS

The carbon structure was formed using SR irradiation at dose of 10000mA min and at a sample temperature of 300 °C. Figure 3 show scanning electron microscopy (SEM) images of carbon structure (a) without SR irradiation region (b) with the SR irradiation region.

As shown in Fig. 3(a), in no SR irradiation region, the carbon film was deposited and the particles were not observed. On the other hand, the deposits with hemispherical shape of nano-meter size were observed on the SR irradiation region as shown in Fig. 3(b).

## REFERENCES


[1] M. Inayoshi *et al*, Jpn. J. Appl. Phys., **34**, L1675 (1995).

[2] M. Inayoshi *et al*, J. Vac. Sci. Technol., **B 17**, 949 (1999).

[3] H. Nagai *et al*, Applied Surface Science **183**, 284 (2001).

[4] H. Nagai *et al*, UVSOR Activity Report 182 (1999).

[5] H. Nagai *et al*, UVSOR Activity Report 216 (2001).

[6] M. Sharon *et al*, J. Power Sources, **104**, 148 (2002).

[7] K. Chakrabarti *et al*, Diamond Relat. Mater., **7**, 845 (1998).

[8] K. Mukhopadhyay *et al*, Phys. Rev. Lett., **72**, 3182 (1994).


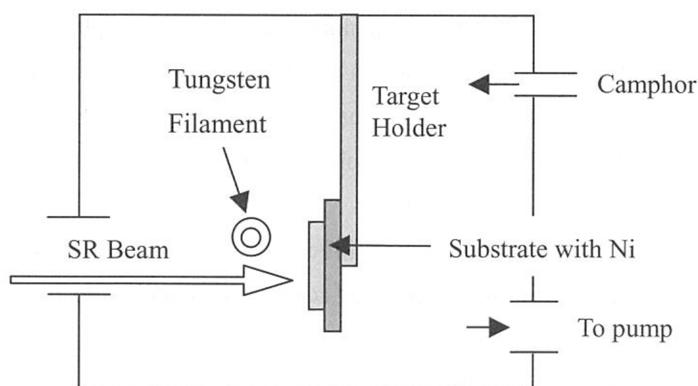


Fig. 1. Experimental set up.

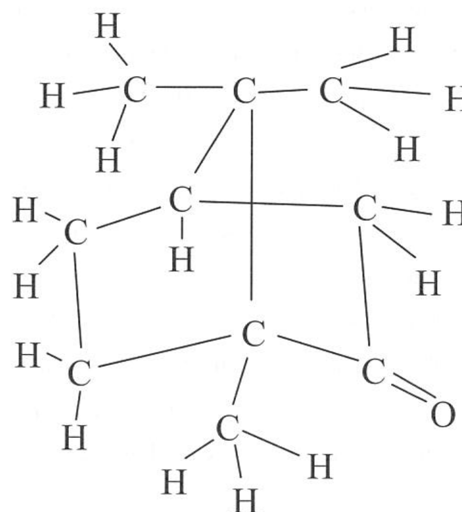


Fig. 2. Structure of Camphor.

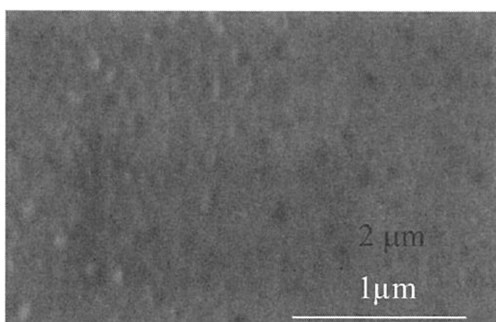


Fig. 3(a). SEM image without the SR irradiation region.

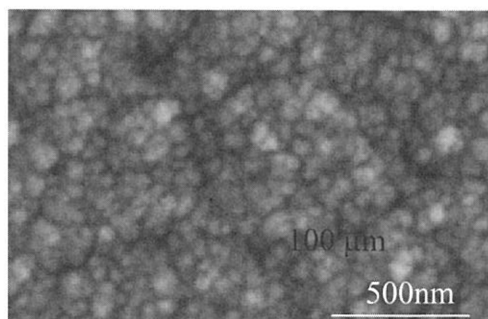


Fig. 3(b). SEM image with the SR irradiation region.

(BL8A)

# Decomposition and Deposition of PTFE by Synchrotron Radiation

H.Okada, E.Matsumoto, H.Yamada, A.Yoshida and A.Wakahara

*Department of Electrical and Electronic Engineering, Toyohashi University of Technology, Tempaku-cho, Toyohashi 441-8580, Japan*

Thin film formation of polytetrafluoroethylen (PTFE) by synchrotron radiation (SR) beam irradiation was studied. In viewpoint of engineering, PTFE has variety of applications due to their superior chemical stability, high thermal stability, high hydrophobicity and low surface tension. It is a key issue for PTFE application to develop a thin PTFE film formation process. Kato's group demonstrated that vacuum ultraviolet light in SR beam has a potential for decomposition of PTFE[1]. They also showed PTFE deposition was achieved by SR beam induced process. In this study, to further investigate decomposition and deposition mechanism of PTFE by SR beam irradiation, atmospheric gas analysis during PTFE decomposition by quadrupole mass spectrometry (QMS) was made for various SR photon fluxes. Photon flux dependence on the quality of deposited film was investigated by Fourier transformation of infrared (FT-IR).

In this study, decomposition and deposition of PTFE were carried out using vacuum chamber connected to BL8A of UVSOR. As shown in Fig.1, SR beam decomposition of PTFE was achieved by direct irradiation of SR beam onto the PTFE target. Deposition of PTFE was achieved by evaporation of decomposed PTFE onto Si (100) substrate that is faced to the target. Atmospheric gas was monitored by QMS during decomposition of PTFE by changing SR beam photon flux of $1.5 \times 10^{17}$ to $1.0 \times 10^{20}$ /s/cm$^2$.

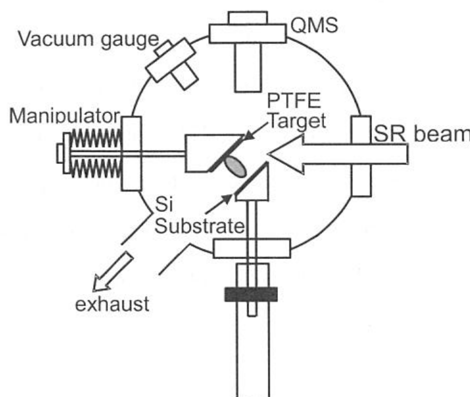


Fig.1: Schematic of experimental setup for decomposition/deposition of PTFE by SR beam.

Table 1: QMS spectrum during PTFE decompostion.

| Photon flux[/s/cm$^2$] \ Species | CF 31 | $CF_2$ 50 | $CF_3$ 69 | $C_2F_3$ 81 |
|---|---|---|---|---|
| $1.7\times10^{17}$(250°C) | 1 | 100 | 8 | 2 |
| $5.8\times10^{19}$(250°C) | 16 | 5 | 100 | 0 |
| $5.9\times10^{19}$(RT) | 11 | 3 | 100 | 0 |
| $F_2$ laser (R.T.)[1] | 100 | 25 | 16 | 6 |
| KrF laser (R.T.)[1] | 100 | 25 | 14 | 6 |
| Test gas $C_3F_8$[2] | 31 | 6 | 100 | 0 |
| $C_4F_{10}$[2] | 26 | 4 | 100 | 0 |
| $C_2F_2$[2] | 100 | 23 | 2 | 24 |

1) T.Katoh and Y.Zhang, Appl.Phys.Lett.68,865(1996)
2)D.R.Weeler and S.V.Pepper, J.Vac.Sci.Technol.A8, 4046

QMS spectra of atmospheric gas during SR beam induced decomposition of PTFE are summarized in Table 1. In this table, reported QMS spectrum during $F_2$- and KrF-laser ablation of PTFE are shown. Adding to this, QMS spectrum pattern of test gas of $C_3F_8$, $C_4F_{10}$ and $C_2F_2$ are also shown. Due to the breaking up of fluorinated carbon in ionization chamber of QMS detector head, small fragments are seen in QMS pattern of test gases. Similar QMS spectra were obtained by SR beam irradiation of photon flux of $5.8x10^{19}$ /s/cm$^2$ at RT and photon flux of $5.9x10^{19}$ /s/cm$^2$. These patterns are different from the QMS pattern from laser ablation, but resemble to $C_3F_8$ and $C_4F_{10}$ test gas pattern. This result suggests that SR beam decomposition of PTFE bears saturated fluorinated carbons, $C_nF_{2n+2}$, by higher photon flux SR beam irradiation. On the other hand, QMS pattern obtained by irradiation of SR beam photon flux of $1.7x10^{17}$ /s/cm$^2$ at 250°C not only different with QMS pattern from laser ablation, but also different with QMS pattern from SR beam irradiation with higher photon flux. Thus, different mechanism is thought between low flux and high flux SR beam irradiation.

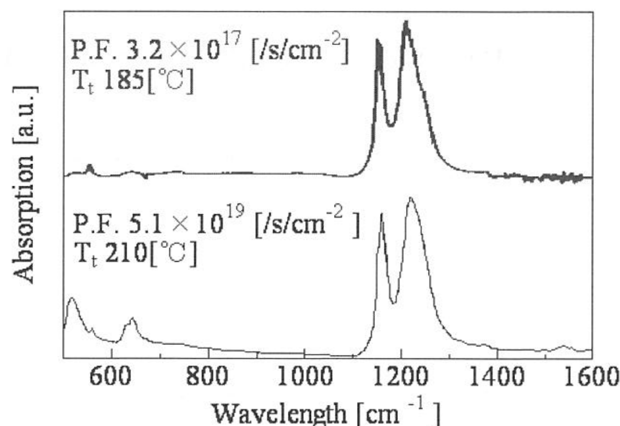


Fig.2: FT-IR spectrum of deposited PTFE.

Figure 2 compares two FT-IR spectra from deposited PTFE formed by SR beam induced evaporation. Wavelength at around 1200 cm$^{-1}$, both FT-IR spectra showed similar peak related to $CF_2$ component in the deposited films. At around 600 cm$^{-1}$ peaks are clearly found in deposited film with photon flux of $5.1x10^{19}$ /s/cm$^2$, however, peaks are quite small in deposited film with photon flux of $3.2x10^{17}$ /s/cm$^2$.

Observed difference in the QMS spectrum of atmospheric gas during decomposition and the FT-IR spectrum of deposited film could be explained by re-polymerization of decomposed PTFE fraction. Base pressure of the reaction chamber is below $1x10^{-7}$ Torr before SR beam irradiation, however, during SR beam induced decomposition with photon flux of $3.2x10^{17}$ /s/cm$^2$, chamber pressure went up to $10^{-4}$ Torr which was monitored by ionization gauge as shown in Fig.1. Much higher pressure should be found above the PTFE target. In such a case, a mean free path in between the target and Si substrate becomes shorter and interaction between decomposed fragments cannot be neglected. Namely, deposited films by higher SR photon flux irradiation are thought to contain intermediates, which cause a difference in QMS spectrum and FT-IR spectrum of high and low flux irradiation of SR beam.

## References

1) T.Kato and Y.Zhang: Appl. Phys. Lett. 68 865 (1996).

2) D.R.Weller and S.V.Pepper: J. Vac. Sci. & Technol. A8, 4046 (1990).

(BL8A)

# Synchrotron radiation-excited etching of ZnTe

Tooru Tanaka, *Kazuki Hayashida, *Yusuke Kume, *Sinji Tokunaga, *Mitsuhiro Nishio, *Qixin Guo, and Hiroshi Ogawa

*Synchrotron Light Application Center, Saga University, Saga 840-8502, Japan*

**Department of Electrical and Electronic Engineering, Faculty of Science and Engineering, Saga University, Saga 840-8502, Japan*

Lowering of the process temperature has recently become more important in fabricating future semiconductor devices such as quantum-effect devices, since the conventional high temperature process brings out the serious deterioration of the device performance due to the disturbance of atomic distribution through the solid-state diffusion. Photo-excited process such as epitaxial growth, etching and surface cleaning is considered as one of the leading candidates for the low temperature process, which also results in the low-damage process. Synchrotron radiation (SR) is an ideal light source for the photo-excited process because its high intensity, small divergence, and continuity of wavelength from the x-ray to the infrared lead to the photo-excitation of most gas molecules and solids used in the semiconductor processes, and provide area-selective microfabrication with high spatial resolution. From these viewpoints, many studies on the technological utilization of SR-stimulated reactions, such as chemical vapor deposition[1,2], etching[3-6], and epitaxy [7-9] have been carried out so far. Concerning the SR-excited etching, the materials for integrated circuit such as Si, $SiO_2$, SiC, and etc, have been studied actively using $SF_6$ as a reaction gas[3-6]. In contrast, the etching of compound materials such as III-V and II-VI semiconductors have not been realized yet in spite of their importance in optoelectronic application. In this study, we have demonstrated the SR-excited etching of ZnTe using $SF_6$ and Ar gas.

The experiments were performed in BL-8A line in UVSOR. The wavelength of the white light at BL-8A port was ranged from x-ray to visible light. The electric current for this SR emission in the storage ring was varied up to 220 mA. The incident beam was introduced perpendicular to the surface of ZnTe (100) substrate through the Ni mesh mask with the hole of $200 \times 200$ μm. After the reaction chamber was evacuated to less than $10^{-7}$ Torr, the reaction gas was fed into the chamber The pressure in the reaction chamber was ranged from $10^{-2}$ to $10^{-1}$ Torr. In the case of Ar gas, the substrate was negatively biased against the reaction chamber. A large pressure difference was sustained between the beam line and the reaction chamber using a differential vacuum pumping system.

In the case of $SF_6$ gas, the surface of ZnTe was not etched, and in stead, a Zn-F compound with the thickness of 20nm was deposited on the substrate, which was confirmed by Auger electron spectroscopy measurement. This may be due to the fact that the vapor pressure of $ZnF_2$ is very low while that of $TeF_6$ is very high, resulting in a formation of $ZnF_2$ on the surface of ZnTe. In the case of Ar gas, we found that the ZnTe was etched by SR beam on the limited area of the surface through a patterned mask under the negative bias to the sample, as shown in Fig.1 and Fig.2. The etching rate was around $4.5 \times 10^{-2}$ Å /mAmin, and it would be expected to improve by optimizing the etching condition such as pressure and bias voltage.

In summary, the SR-excited etching of ZnTe was achieved using Ar gas with negative bias to the sample in this experiment for the first time.

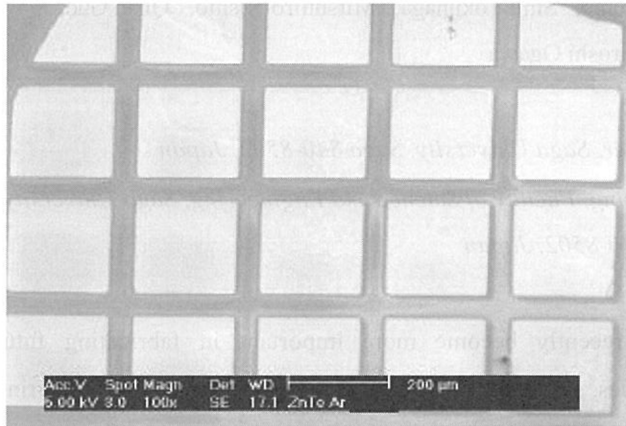


Fig.1. SEM photograph of ZnTe etched in Ar atmosphere under negative bias to the sample.

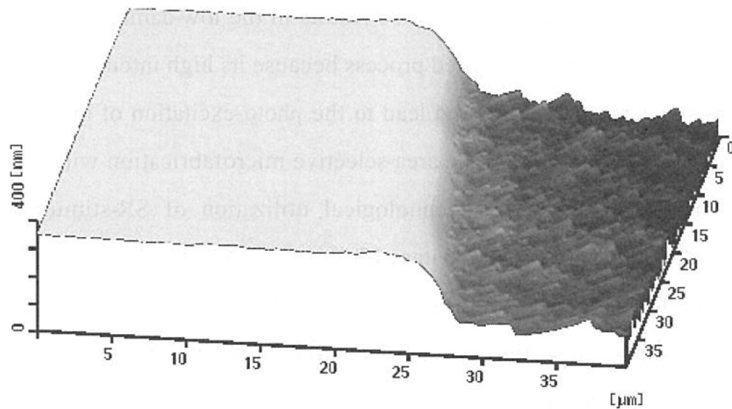


Fig.2. AFM image of ZnTe surface etched in Ar atmosphere under negative bias to the sample.

## References


[1] D. C. Mancini, S. Varma, J. K. Simons, R. A. Rosenberg, and P. A. Dowben, J. Vac. Sci. Technol. B 8, 1804 (1990).

[2] D. Byun, S. D. Hwang, P. A. Dowben, F. K. Perkins, F. Filips, and N. J. Ianno, Appl. Phys. Lett. 64, 1968 (1994).

[3] Y. Utsumi, J. Takahashi, and T. Urisu, J. Vac. Sci. Technol. B 9, 2507 (1991).

[4] S. Terakado, O. Kitamura, S. Suzuki, and K. Tanaka, J. Vac. Sci. Technol. B 11, 1890 (1993).

[5] K. Shobatake, H. Ohashi, K. Fukui, A. Hiraya, N. Hayasaka, H. Okano, A. Yoshida, and H. Kume, Appl. Phys. Lett. 56, 2189 (1990).

[6] H. Ohashi, A. Yoshida, K. Tabayashi, and K. Shobatake, Appl. Surf. Sci. 69, 20 (1993).

[7] Y. Nara, Y. Sugita, K. Horiuchi, and T. Ito, Appl. Phys. Lett. 61, 93 (1992).

[8] J. Takahashi, Y. Utsumi, H. Akazawa, I. Kawashima, and T. Urisu, Thin Solid Films 218, 40 (1992).

[9] H. Akazawa, Y. Utsumi, T. Urisu, and M. Nagase, Phys. Rev. B 47, 15946 (1993).

(BL8A)

# Synchrotron Radiation Beam Induced Etching of Polymers for Microfabrication

A.Yoshida, E.Matsumoto, H.Yamada, H.Okada and A.Wakahara

*Department of Electrical and Electronic Engineering, Toyohashi University of Techonology, Tempaku-cho, Toyohashi, 441-8580, Japan*

Polymers which include polytetrafluoroethylene (PTFE), polyimide etc., have been paid attentions due to their exceptional properties. Their high chemical stability, low friction surface properties high insulation ability are quite useful for microelectronics or MEMS. For such application, microfabrication technology of those polymers having precise controllability is important. Synchrotron radiation (SR) induced processing has a potential for such precise microfabrication, because SR beam is a high photon energy with collimated light. In this study, etching of polymers, particulary PTFE and polyimide, by SR beam exposure have been investigated aiming future microfabrication of polymers.

Figure 1 shows experimental setup for SR induced etching. Target PTFE/polyimide bulk is mounted on the target holder that is placed in the vacuum chamber. The chamber was evacuated with turbo molecular pump below $1x10^{-6}$ Torr. Etching of polymers was made by exposure of SR beam on the target. In this study etching rate dependence on target temperature and SR photon flux (P.F.) were investigated.

SR beam etching of PTFE was clearly observed in this study. On the other hand, no clear etching but surface modification of polyimide was seen. Figure 2 shows dependence of PTFE etching rate on the target temperature. Etching rate was increased with increase of target temperature. This result suggests that heating of target enhances decomposition of PTFE. Etching was also enhanced with higher photon flux exposure.

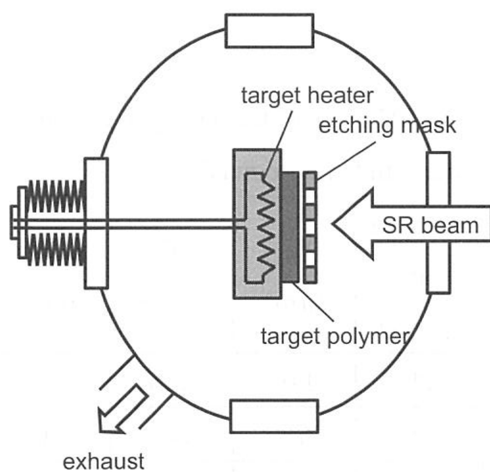


Fig. 1: Experimental setup.

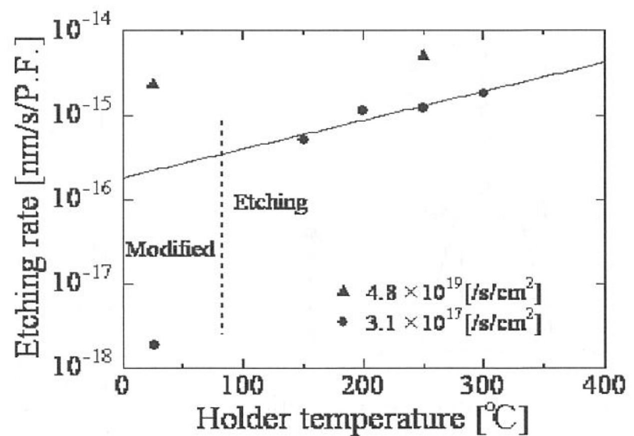


Fig.2: Etching rate dependence on target holder temperature.

For low photon flux exposure of SR beam (P.F.=3.1x10$^{17}$ /s/cm$^2$) at RT, however, no clear etching was but surface modification was observed. This suggests that some critical temperature exists on PTFE etching by low SR photon flux. On the other hand, with higher SR beam exposure (P.F.=4.8x10$^{19}$ /s/cm$^2$), PTFE etching was achieved even at RT. This could be explained by heating up of PTFE target induced by SR beam exposure.

Due to the collimation of SR beam, etched structure having large steepness are expected. To investigate this point, Cu wire having a diameter of 0.1μm was used as a mask of PTFE etching. After the etching by SR beam exposure, a wall structure of PTFE was obtained underneath the Cu wire. Here, effects of exposed photon flux and target temperature on the etched structure were studied. Dimensions of wall structure which includes top ($W_T$) and bottom width ($W_B$), and steepness of delineated wall defined by $(W_B+W_T)/t$, where $t$ is the target thickness are summarized in Table 1. Dependence of the dimensions on the holder temperature and photon flux were observed. Both of the top and bottom width decreased with higher photon flux and higher target temperature. Observed decrease of bottom width ($W_B$) is thought as an advance of etching which give rise on unmasked part. Rather small steepness in lower photon flux and lower target temperature can be explained by incomplete etching on backside of PTFE. Top width ($W_T$) also decreased with higher photon flux and higher target temperature etching. In Table 1, smaller top width as compared with wire width was observed after the etching with photon flux of 2.3x10$^{19}$ /s/cm$^2$ at 250°C. Furthermore, with photon flux of 6.0x10$^{19}$ /s/cm$^2$ exposure, a break off of the wall was observed. These results can be explained by increase of lateral etching of PTFE. One possibility is that higher photon flux exposure causes partial rising of the target temperature. Such heat up affects the edges of masked PTFE portion. This point is consistent with observed etching rate dependence on the target temperature shown in Fig.1.

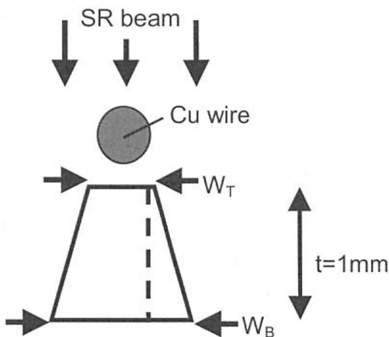

Fig.3: Schematic cross-section of PTFE etching using Cu wire mask.

Table 1: Dimensions of PTFE wall formed by SR beam exposure with Cu wire mask.

| P.F. (/s/cm$^2$) | $T_t$ (℃) | etching rate (μm/s) | $W_T$ (μm) | $W_B$ (μm) | Steep-ness |
|---|---|---|---|---|---|
| 2.8x10$^{19}$ | RT | 29 | 110 | 250 | 14 |
| 4.4x10$^{13}$ | RT | 48 | 78 | 130 | 40 |
| 2.3x10$^{19}$ | 250 | 58 | 87 | 115 | 66 |
| 6.0x10$^{19}$ | 250 | 148 | x | x | x |